

Modeling precursory laboratory seismicity using a wear-based rate- and state-dependent friction model

Paul Antony Selvadurai¹, Percy Galvez², P. Martin Mai², Steven Glaser³, and Stefan Wiemer⁴

¹ETH Zurich

²King Abdullah University of Science & Technology

³University of California, Berkeley, CA

⁴ETH

November 24, 2022

Abstract

We develop a rate- and state-dependent friction (RSF) model to investigate a compendium of recent experiments performed in the laboratory. In the documented experiments, a fault was sheared until macroscopic stick-slip frictional failure. Before macro-failure, small precursor seismicity nucleated from regions that also experienced aseismic slow slip. This behavior requires heterogeneity and is defined in our model as local variation in frictional parameters inferred from the roughness. During sliding wear introduced a smooth-polished surface onto a previously rough surface and was quantified using a bimodal Gaussian distribution of surface heights. We used spatial distribution of the smooth and rough sections to impose binary partitioning in critical slip distance D_c to a planar frictional model. Simulations revealed that local seismicity nucleated on the “smooth” sections, while the larger “rough” section hosted aseismic slip. As the level of heterogeneity between smooth and rough sections increased, the model transitioned from a predominantly stick-slip to creeping. The simulations produced a dominant asperity, which appeared to control aspects of rupture nucleation: (i) weak heterogeneity caused the dominant asperity to generate foreshocks but also “ignite” cascade-up fault-wide event, while (ii) strong heterogeneity led to constrained repeaters. Seismic source properties: average slip δ , seismic moment M_0 , stress drop $\Delta \tau$ and fracture energy G^* , were determined for each event and agreed with separate kinematic estimates made independently from seismic measurements. Our numerical calculations provide insight into rate-dependent cascade-up nucleation theory where frictional heterogeneity here was associated with wear of solid frictional contacts in the laboratory.

1 **Modeling precursory laboratory seismicity using a**
2 **wear-based rate- and state-dependent friction model**

3 **P. A. Selvadurai¹, P. Galvez², P. M. Mai², S. D. Glaser³, S. Wiemer¹**

4 ¹Swiss Seismological Service, ETH Zurich, Zurich, Switzerland

5 ²King Abdullah University of Science and Technology, Thuwal, Saudi Arabia

6 ³Civil and Environmental Engineering, University of California, Berkeley, California, USA

7 **Key Points:**

- 8 • Rate and state friction models prescribed D_c based on roughness measurements that
- 9 displayed clear signs of wear
- 10 • Polished sections initiated seismicity and controlled stick-slip-dominant to creep-
- 11 dominant behaviors
- 12 • A dominant “mirror” section was found to control foreshocks and possessed the po-
- 13 tential to ignite runaway rupture

Corresponding author: Paul Selvadurai, paul.selvadurai@sed.ethz.ch

14 **Abstract**

15 We develop a rate- and state-dependent friction (RSF) model to investigate a compendium
 16 of recent experiments performed in the laboratory. In the documented experiments, a fault
 17 was sheared until macroscopic stick-slip frictional failure. Before macro-failure, small precursor
 18 seismicity nucleated from regions that also experienced aseismic slow slip. This behavior
 19 requires heterogeneity and is defined in our model as local variation in frictional parameters
 20 inferred from the roughness. During sliding wear introduced a smooth-polished surface
 21 onto a previously rough surface and was quantified using a bimodal Gaussian distribution
 22 of surface heights. We used spatial distribution of the smooth and rough sections to impose
 23 binary partitioning in critical slip distance D_c to a planar frictional model. Simulations
 24 revealed that local seismicity nucleated on the “smooth” sections, while the larger “rough”
 25 section hosted aseismic slip. As the level of heterogeneity between smooth and rough sections
 26 increased, the model transitioned from a predominantly stick-slip to creeping. The
 27 simulations produced a dominant asperity, which appeared to control aspects of rupture
 28 nucleation: (i) weak heterogeneity caused the dominant asperity to generate foreshocks but
 29 also “ignite” cascade-up fault-wide event, while (ii) strong heterogeneity led to constrained
 30 repeaters. Seismic source properties: average slip δ , seismic moment M_0 , stress drop $\Delta\tau$
 31 and fracture energy G' , were determined for each event and agreed with separate kinematic
 32 estimates made independently from seismic measurements. Our numerical calculations provide
 33 insight into rate-dependent cascade-up nucleation theory where frictional heterogeneity
 34 here was associated with wear of solid frictional contacts in the laboratory.

35 **Keywords:** Earthquake nucleation, foreshocks, laboratory experiments, rate and state
 36 friction, wear, asperities, seismic source properties

37 **Plain Language Summary**

38 Recent seismic observations show that faults experience a range of slip patterns spanning
 39 many scales in both space and time. From faults that can creep slowly to those that
 40 slip suddenly and release large amounts of energy. Understanding how large and small faults
 41 unlock require us to develop models that can produce a range of behavior and characteristics.

42 Foreshocks are observed in regions that have been found to host large devastating earthquakes
 43 but are not well understood. Understanding when, where and how foreshocks appear,

44 in relation to its mainshock, surrounds the study of earthquake nucleation. Heterogeneity
45 is believed to be a necessary ingredient for foreshocks to occur.

46 We developed a model to explain laboratory experiments that noticed wearing (pol-
47 ishing) of fault surfaces that also produced foreshocks. Our model used the mirror-finished
48 sections to impose spatial heterogeneity and investigated how varying its properties con-
49 trolled the faults response. We captured a range of typical seismic behaviors from repeating
50 earthquakes, to foreshocks, to earthquakes that originated at very small scales and possessed
51 the potential to ignite and cascade-up into large system wide events.

52 **1 Introduction**

53 Seismologic observations have captured a growing diversity in slip behavior along natu-
54 ral faults. Observations, such as spatio-temporal variations in seismicity rates (Tormann et
55 al., 2014, 2015; Gulia et al., 2016; Gulia & Wiemer, 2019), the presence of repeaters in aseis-
56 mically creeping fault sections (e.g. Nadeau et al., 1994; Nadeau & McEvilly, 1999; Shirzaei
57 & Bürgmann, 2013; Uchida, 2019), variations of slow slip distribution over large scales in-
58 ferred from geodetic measurement (e.g. Brodsky & Lay, 2014; Ruiz et al., 2014; Socquet
59 et al., 2017), the earthquake potential on sections prone to large ruptures (Bürgmann et
60 al., 2000; Bürgmann, 2004), the observed variability in spatio-temporal slip patterns during
61 rapid rupture (e.g. Mai & Beroza, 2002; Tinti et al., 2005; Dreger et al., 2007; Galvez et
62 al., 2016; Mai et al., 2018) suggest that coupling of faults and the ability to resist frictional
63 breakdown is heterogeneous.

64 Heterogeneity in frictional properties is also necessary to explain the observation that,
65 in certain cases, precursory seismicity has been detected in regions that also support the
66 steady growth of a preslip region (A. Kato et al., 2012, 2016; Obara & Kato, 2016; Ruiz
67 et al., 2014; Bouchon et al., 2013; Bürgmann, 2004). Preslip is a slow accumulation of
68 fault slip in a region that grows outwards to a critical size where it becomes unstable and
69 the mainshock ensues (Mogi, 1985; Ohnaka, 1992; Ben-Zion, 2008). This portion of the
70 seismogenic cycle is known as the nucleation phase. This behavior has been identified from
71 the onset of the mainshock’s seismogram (Iio, 1995; Ellsworth & Beroza, 1995; Beroza &
72 Ellsworth, 1996), whilst recent improvements in geodetic measurements help to lower the
73 detectable threshold and identify the nucleation phase over long time scales (months to
74 years) and length scales (kms) (e.g., Roeloffs, 2006; Wang & Bilek, 2014; Ruiz et al., 2014;

75 Socquet et al., 2017). In certain cases, precursory seismicity in the form of foreshocks has
76 been observed prior to the mainshock (e.g., Dodge et al., 1995, 1996; Bouchon et al., 2011).
77 While it is unclear if all mainshocks are preceded by foreshocks (Brodsky & Lay, 2014;
78 Mignan, 2014; Seif et al., 2018) they are currently only identifiable in retrospective analysis.
79 Due to their forecasting potential, foreshocks have become important phenomena to study.

80 The study of the spatio-temporal growth of a preslip region and its transition from slow
81 (quasi-static) to fast (dynamic) slip has been well documented in laboratory experiments
82 (Dieterich, 1978; Okubo & Dieterich, 1984; Ohnaka & Shen, 1999; Nielsen et al., 2010;
83 Latour et al., 2013; Fukuyama et al., 2018; Zhuo, Guo, et al., 2018; Ke et al., 2018; Buijze
84 et al., 2020). More recently, along with measuring the spatio-temporal evolution of a slow
85 preslip region, acoustic emission sensors were deployed to detect localized, high-frequency
86 and impulsive events that spontaneously emanate from sections of the fault that also hosted
87 the preslip region (Ma et al., 2002; McLaskey & Kilgore, 2013; McLaskey & Lockner, 2014;
88 Selvadurai & Glaser, 2015a; Passelègue et al., 2017; Zhuo, Liu, et al., 2018). Analysis of
89 these localized events using seismological models found the moment released with respect
90 to their geometry scaled with earthquakes in nature (McLaskey et al., 2014; Selvadurai,
91 2019). This similarity has sparked more interest in understanding the implications that
92 laboratory foreshocks have on the growth and stability of the preslip region and the influence
93 of foreshocks themselves on the size and timing of the larger mainshock (McLaskey, 2019).

94 A major question is when does a foreshocks ‘cascade-up’ into the mainshock? Studies of
95 the initial onset of seismic rupture using seismograms suggest that asperities exist at many
96 spatial scales, and that the triggering of a cascading-style failure mechanism might stem
97 from failure of a smaller section (Okuda & Ide, 2018a; Ide, 2019). This type of hierarchical
98 breakdown may indicate the existence of a hierarchical plate interface structure (Ide &
99 Aochi, 2005; Aochi & Ide, 2014, 2017). Foreshocks might be local failures of these asperities
100 that do not fully ‘cascade-up’ but possess ‘runaway potential’ if conditions are favourable.

101 Conditions that controls the occurrence of foreshocks (or other types of precursory
102 seismicity) during the nucleation phase, even at laboratory scales, is not entirely clear. In
103 previous laboratory foreshocks studies (McLaskey & Kilgore, 2013; Selvadurai & Glaser,
104 2015a), frictional fault behavior was dictated by a dry and gouge-free fault environment. In
105 these cases, heterogeneity is believed to occur because of geometric interaction between two
106 rough surfaces that give rise to contact asperities with locally high normal stresses. The

107 contact heterogeneity was confirmed by Selvadurai and Glaser (2017) with measurement of
108 spatially variable normal stress determined from a pressure sensitive film placed along the
109 interface; this has also been widely investigated in the field of statistical contact mechanics
110 (e.g. Greenwood & Williamson, 1966; Johnson, 1985; Persson, 2006).

111 The relationship between contact heterogeneity and mechanisms explaining sponta-
112 neous occurrence of foreshocks in sections of accumulating slip were examined. Selvadurai
113 and Glaser (2017) proposed that localized precursory events occurred on asperities that ex-
114 hibit higher levels of normal stress, thus locally decreasing its critical nucleation length scale
115 (defined later in Section 2.1). If the asperity was geometrically large enough with locally high
116 normal stress, favorable conditions allowing for the spontaneous localization of foreshocks
117 could occur in the preslip region. This hypothesis is also discussed by McLaskey (2019).
118 Another mechanism proposed by McLaskey and Kilgore (2013) was that the increased stress-
119 ing rate around the local geometric interference between surfaces might contribute to higher
120 shear stresses resulting in the dynamic failure of these contact asperities.

121 But why do the foreshocks arrest? What type/level of frictional heterogeneity is nec-
122 essary to arrest the rupture that should, on a homogeneous interface, continue to rupture
123 over the entire frictional interface? From the study of dynamic rupture propagation, after
124 spontaneous initiation of dynamic rupture, the slip front begins to expand in a crack-like
125 manner, accelerating outwards to a critical velocity, whereby it may transition to a pulse-like
126 dynamic rupture (Heaton, 1990; Meier et al., 2016). Experiments and numerical investiga-
127 tions into the causes of complex rapid rupture nucleation and arrest in the laboratory are
128 highly dependent on the stress states on the fault ahead of the rupture (Rubinstein et al.,
129 2004, 2006; Ben-David et al., 2010; Svetlizky & Fineberg, 2014; Fineberg & Bouchbinder,
130 2015; Maegawa et al., 2010; Trømborg et al., 2011; Kammer et al., 2012; ?, ?; Kammer et al.,
131 2015) and appear to control even slower quasi-static ruptures (Selvadurai et al., 2017). The
132 study of why/how laboratory ruptures arrest in these studies are performed at larger scales
133 and do not study the high-frequency emissions measured using acoustic emission sensors.
134 For this reason, it becomes difficult to investigate the interaction of the foreshock/nucleation
135 region which requires, in the laboratory, a broadband temporal and spatial understanding
136 of slip: from frequencies ranging from DC to ~ 1.5 MHz and length scales ranging from tens
137 of microns to meters.

138 In this study, we aim to understand mechanisms for localized fast ruptures embedded
 139 within a slow rupture where asperities are formed from geometric mismatch of the two
 140 rough surfaces. We apply a numerical rate- and state-friction (RSF) model (Dieterich,
 141 1979; Ampuero & Rubin, 2008; Rubin & Ampuero, 2005) to explain a compendium of
 142 laboratory data from a specific direct shear friction experiment performed on a fault analog.
 143 The observations follow recent publications the reader may consult for experimental details,

- 144 1. Selvadurai and Glaser (2015a) looked at the nucleation phase where a slow preslip
 145 front was observed prior to onset of system wide stick-slip instabilities. Within this
 146 preslip region, localized foreshocks were observed;
- 147 2. Selvadurai and Glaser (2017) investigated characteristics of the roughness and quan-
 148 titative analysis of the contact stresses on the asperities were documented;
- 149 3. Selvadurai (2019) estimated seismic source properties of the localized foreshocks
 150 events that occurred in the preslip nucleation region were quantified using kinematic
 151 source models.

152 1.1 Summarized Experiment

153 A schematic diagram of the direct shear friction apparatus is presented in Figure 1(a).
 154 We refer to this scale as the macroscopic scale for the discussion. Experiments consisted
 155 of loading a long slender polymethyl methacrylate (PMMA) slider onto a larger PMMA
 156 base plate; the interacting faces were first sandblasted. During an experiment, the fault
 157 was maintained under constant normal load F_n . The top slider was driven at a constant
 158 macroscopic loading rate V_{LP} and an in-line shear load cell was used to measure the bulk
 159 frictional resistance F_S along the fault (see Figure 1(b)).

160 In Figure 1(b) the slip evolution (black line) for the stick-slip event as measured by the
 161 non-contact eddy current sensor (NC5). Figure 1(c) depicts a schematic representation of
 162 the eddy current sensor (mounted on the base plate) and the wing target attached to the
 163 slider block ~ 2.5 mm above the interface. The inductive eddy current sensors measured
 164 slip δ in the x -direction. We refer to this scale as the mesoscopic scale for the discussion.

165 During a stick-slip cycle, the slow and smooth accumulation of aseismic slip is detailed
 166 in Figure 1(d); lines of constant slip rate (magenta) are superimposed over the slip evolution
 167 curve. The fault displayed an acceleration of aseismic slip leading to the stick-slip event. This

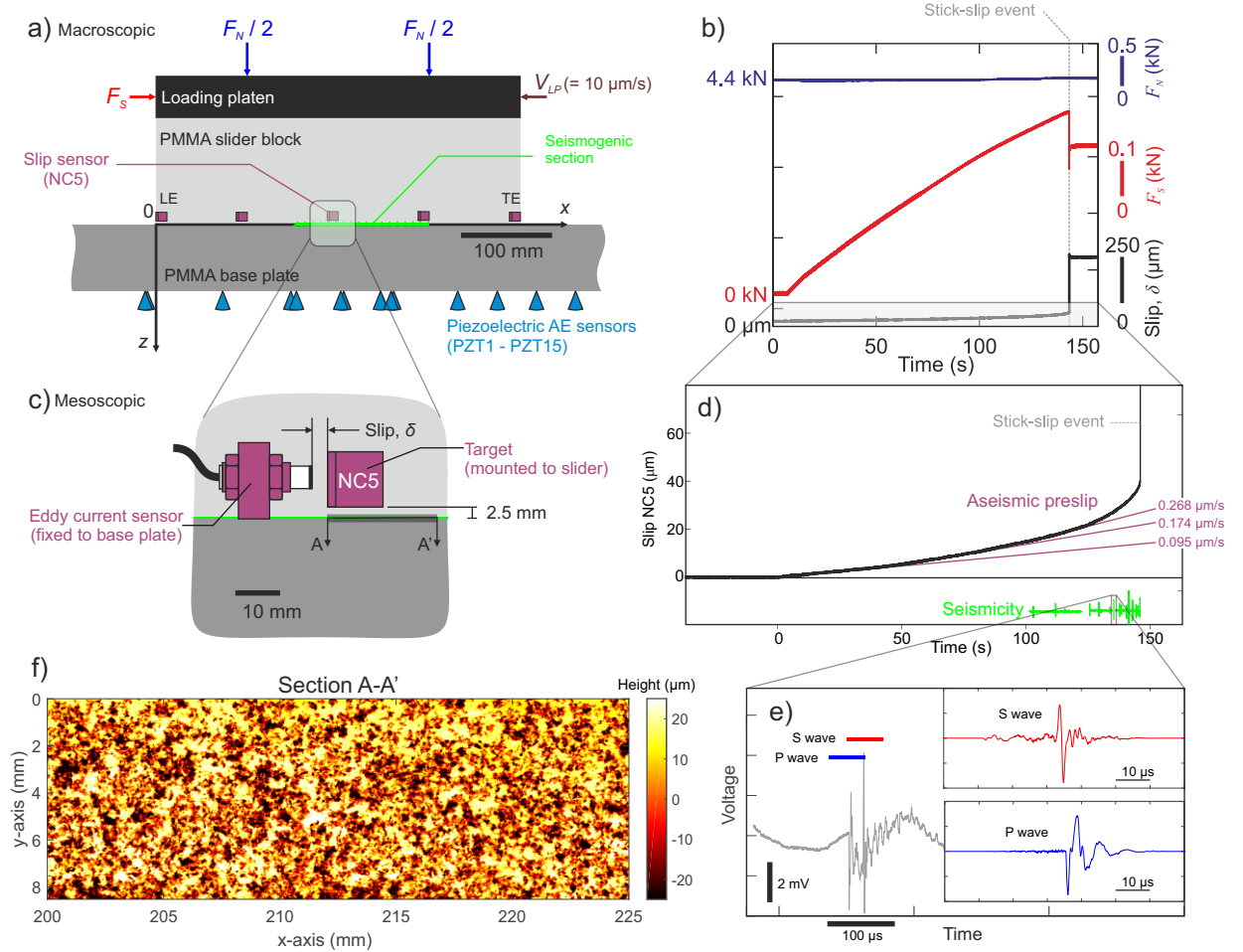


Figure 1. (a) Schematic details of the direct shear friction apparatus depicting the general loading conditions and sensor placements are displayed. For more technical details please consult Selvadurai and Glaser (2015b). (b) Typical result demonstrating the bulk frictional evolution in terms of shear slip and shear force leading up to failure. (c) Schematic details of the non-contact eddy current sensor placement at the mesoscopic scale. (d) Detailed slip measurement during the experiment presented in (b). Mesoscopic slow aseismic slip was observed prior to macroscopic stick-slip failure. Lines of constant slip velocity are displayed for reference. Seismicity (green) is represented schematically to document presence of local fast slip as the accelerated aseismic slip was observed. (e) Example of precursory seismicity recorded using PZT7. Seismicity showed clear P and S wave arrivals. More detailed source analysis has been performed by Selvadurai (2019). (f) Surface roughness measurement taken *a posteriori* using the longer length scale optical profilometer (Selvadurai & Glaser, 2017). The region on the fault associated with this scan is highlighted by the cross-section A-A' in (c).

168 type of observation is fairly common in laboratory friction experiments. However, we also
 169 observed pronounced impulsive events, detected using an array of calibrated piezoelectric
 170 transducers (PZT) that measure high-frequency vibrations (100kHz to 1500 kHz) produced
 171 by seismic stress waves. Seismicity is represented schematically (green) since the time scales
 172 between the slow slip and this impulsive source were ~ 6 orders of magnitude different.
 173 Figure 1(e) depicts isolated P and S waves from a typical impulsive source measured by
 174 PZT7 (Selvadurai, 2019).

175 Our friction model requires spatial heterogeneity to explain the observations of syn-
 176 chronous and concomitant slow (Figure 1(d)) and fast rupture (Figure 1(e)). In our RSF
 177 model we base spatial heterogeneity on the experimental *a posteriori* measurement of sur-
 178 face roughness. Figure 1(f) presents the optical scan of surface roughness on the top slider
 179 block surface through the cross-section A-A' in Figure 1(c). The scan was taken below the
 180 non-contact sensor NC5.

181 1.2 Surface Roughness Analysis

182 Roughness has been proposed as a controlling feature linked to variability in frictional
 183 behavior on faults (Scholz & Aviles, 1986; Scholz, 2002). Studies of the roughness of large
 184 exposed outcrops have been used to develop models describing the heterogeneity in stress and
 185 strength on active faults (e.g., Schmittbuhl et al., 2006). Large sections of exposed faults
 186 exhibit variability in roughness, which can be characterized using various measurements
 187 techniques (Power & Tullis, 1991; Schmittbuhl et al., 1995; Renard et al., 2006; Candela
 188 et al., 2009; Brodsky et al., 2011; Siman-Tov et al., 2013; Kirkpatrick & Brodsky, 2014;
 189 Candela & Brodsky, 2016; Brodsky et al., 2016). We briefly describe methods used to
 190 quantify surface roughness in the fields of contact mechanics, tribology and geophysics that
 191 we will then use to characterize the interface presented in Figure 1(f). We measure average
 192 roughness as the root mean square:

$$h_{rms} = \sqrt{\left(\frac{1}{N}\right) \sum_{i=1}^N h_i^2}, \quad (1)$$

193 where N is the total number of measurement points and h_i is the individual surface height.
 194 To estimate statistical properties of surface heights we also employ the probability density
 195 functions (PDFs) of the surface height h defined by a Gaussian distribution, given as follows:

$$\phi(h) = (2\pi\sigma^*) \exp\left[-\frac{(h - \mu^*)^2}{2\sigma^{*2}}\right], \quad (2)$$

196 where μ^* is the arithmetic mean and σ^* is the standard deviation. Building on equation
197 eq1 the PDF for a bimodal Gaussian mixture model is given by

$$\Phi(h) = p \cdot \phi_1(h) + (1 - p) \cdot \phi_2(h), \quad (3)$$

198 where p is the mixture ratio between the two Gaussian distribution functions ϕ_1 and ϕ_2 ,
199 each with their individual means and standard deviations. When fitting eq1 and eq2 to
200 the experimental measurements we employ a maximum likelihood estimation (MLE) of the
201 means, standard deviations and mixture ratio.

202 Finally, we estimate surface properties using power spectral density (PSD), i.e. the
203 square of the modulus of the normalized Fourier transform, of a self-affine surface profile
204 following

$$P(k) \propto k^{-(1+2H)}, \quad (4)$$

205 where k is the wavenumber and H is the self-affine scaling exponent or Hurst exponent
206 (Power & Tullis, 1991; Schmittbuhl et al., 1995; Mai & Beroza, 2002; Candela et al., 2009).
207 By plotting equation eq999 we can estimate H using linear regression of log-log slope of the
208 relationship between the PSD and wavenumber $\beta = -(1 + 2H)$.

209 1.3 Evidence of fault wear

210 The facilities and measurement techniques are discussed in detail by Selvadurai and
211 Glaser (2017). Figure 2(a) displays estimates of surface roughness using the root mean
212 square (16.7 μm using equation eq99), Gaussian (equation eq1) and bimodal Gaussian
213 (equation eq2) distributions for the surface presented in Figure 1(f). The values of the
214 means (μ^*), standard deviations (σ^*) and mixture ratio (p), are given for the modal (ma-
215 genta) and bimodal (cyan), models with units of μm . The shape of the distribution is most
216 adequately characterized by the bimodal Gaussian distribution. Evolution of roughness
217 from Gaussian to bimodal Gaussian can be quantified using the polish-rate decay (wear
218 decay or *Borucki* wear) function (Adachi & Kato, 2000; L. Borucki, 2002; L. J. Borucki

219 et al., 2004; Ciavarella, 2016; He et al., 2017; Hu et al., 2019a). This type of distribution
 220 has been well-documented in the field of tribology and is used to characterize wear of the
 221 interface. As the surface wears from a Gaussian to bimodal Gaussian it reaches a steady
 222 state roughness. This worn characteristic was likely due to the lapping procedure described
 223 in Selvadurai and Glaser (2015a) in which ~ 36.1 mm slip was used to precondition the
 224 originally sandblasted surface before any experiments were reported. We see that wear had
 225 produced a smoother surface (i.e. the ‘tail’ in the PDF), and this polished surface existed
 226 within the encompassing rougher surface.

227 Figure 2(b) marks the Hurst exponent estimated using the power spectral density from
 228 the surface roughness transects in the x -direction. The average PSD was used to estimate
 229 a Hurst exponent $H = 0.43$ between the wavenumbers of $1 \text{ mm}^{-1} < k < 50 \text{ mm}^{-1}$ from
 230 equation eq999. We note that any deviations of the values presented here from those in
 231 Selvadurai and Glaser (2017) are due to the more accurate cropping of the measurement
 232 region presented in Figure 1(f).

233 Figure 2(c) reveals a raw photograph of the surface of the seismogenic section of the
 234 fault (Selvadurai & Glaser, 2017), revealing polished spots with a “mirror-like” finish that
 235 was responsible for the tail in the PDF of the surface roughness. From Selvadurai and
 236 Glaser (2017), the polished surface ‘mirrors’ were 188 times smoother than the overall RMS
 237 roughness for the full region ($h_{RMS} = 16.7 \mu\text{m}$). Figure 2(d) highlights the darker regions
 238 by converting the raw image from RGB to light intensity between the range of $0 < I <$
 239 0.35 (Gonzalez et al., 2009). The inset image displays the complexity associated within the
 240 polished section.

241 The presence of fault-mirrors (FM) observed on natural outcrops have sparked interest
 242 from the geophysical community (Fondriest et al., 2013; Kirkpatrick et al., 2013; Siman-Tov
 243 et al., 2013). Laboratory experiments have been crucial in understanding the mechanism
 244 surrounding the formation of FMs and the debate of whether the presence of a fault mirror
 245 can be used as an indicator of seismic slip (Fondriest et al., 2013; Siman-Tov et al., 2013;
 246 Pozzi et al., 2018), but they have also been reproduced during slow slip (Tisato et al.,
 247 2012; Siman-Tov et al., 2015), in high-temperature environments (Pluymakers & Røyne,
 248 2017) and observed along glacial boundaries (Siman-Tov et al., 2017). Figures 2(e) and
 249 (f) show fault mirrors on the Dead Sea Transform and the Corona Heights Fault (USA),
 250 respectively, that formed at different scales. Goldberg et al. (2016) believe that these FMs

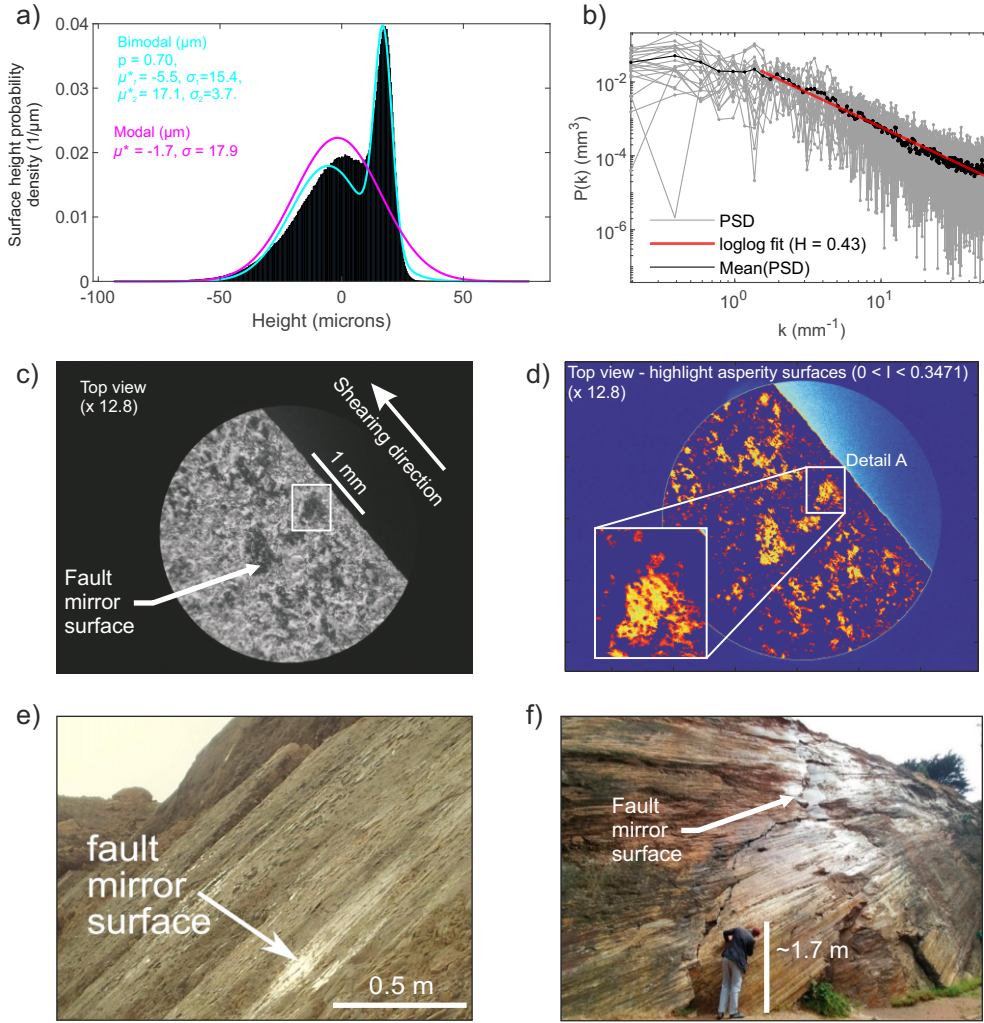


Figure 2. (a) Surface height probability density function for the surface in Figure 1(f). Values of three surface roughness models are established for the root mean square (black), Gaussian (magenta) and bimodal Gaussian (cyan) – the values are given in μm . (b) Estimate of the Hurst exponent from the same surface are estimated from the power spectral density (PSD) described by equation eq999 along the all transects in the x -direction (gray lines). The mean PSD for this surface is displayed in black and the Hurst exponent $H = 0.43$ (red line) was estimated. (c) Image of the worn PMMA fault surface from (Selvadurai, 2015) reveals dark, smooth spots that are indicative of worn sections of the PMMA slider block. (d) Post-processing highlights the darker smooth sections. The inset image displays the spatial complexity of the smooth region. (e) Exposed outcrop with a mirror surface on a fault located along the Dead Sea Transform (image adapted from Goldberg et al. (2016)). (f) Exposed outcrop with striated, glossy surface of the Corona Heights Fault (USA) (adapted from Verberne et al. (2019)).

251 can potentially promote seismicity and can form at lower slip rates than previously thought
 252 (Verberne et al., 2019). While there are differences between the mechanisms controlling how
 253 surfaces polish and FMs develop on rock-rock interfaces in hydro-thermal environments and
 254 controlling their development on a plastic PMMA surface (Bouissou et al., 1998), we are
 255 more interested in how the initial conditions of a “smoother surface embedded in a rougher
 256 fault” affect the frictional dynamics associated with using a RSF model.

257 **2 Rate- and state-dependent (RSF) friction model**

258 **2.1 Theory**

259 The RSF constitutive friction law is phenomenological and derived from laboratory
 260 experiments (Dieterich, 1979; Ruina, 1983). The model describes the behavior of a fault’s
 261 resistance to sliding in terms of shear stress τ as a function of slip rate V and state variable
 262 θ . This is given as:

$$\tau(V, \theta) = \sigma_n \left[\mu + a \ln \frac{V}{V^*} + b \ln \frac{V^* \theta}{D_c} \right], \quad (5)$$

263 where σ_n is the normal stress, μ is the reference steady-state friction coefficient at an arbitrary
 264 reference slip rate V^* , D_c is the characteristic slip distance and a and b are constitutive
 265 parameters describing the direct and evolution effects, respectively. We adopt the state parameter
 266 in the form of the so-called “slip law” because of its ability to model recent
 267 laboratory studies (Bhattacharya et al., 2015; Kaneko & Ampuero, 2011; Kaneko et al.,
 268 2016):

$$\dot{\theta} = -\frac{V\theta}{D_c} \ln \frac{V\theta}{D_c}, \quad (6)$$

269 where friction at steady state ($\dot{\theta} = 0$) is given as

$$\tau_{ss}(V) = \sigma_n \left[\mu + (a - b) \ln \frac{V}{V^*} \right]. \quad (7)$$

270 From equation eq7 we see that constitutive parameters $(a - b)$ play an influential role in
 271 how the interface behaves at steady-state. For $(a - b) < 0$, τ_{ss} will decrease as slip rate V
 272 increases. A fault with these characteristics is known as velocity-weakening (VW) and is
 273 prone to spontaneous instability if the fault stiffness is below a critical stiffness. Stiffness

274 of the VW spring-slider system was investigated by Ranjith and Rice (1999) who found the
 275 critical stiffness to be:

$$k_{cr} = \frac{\sigma_n (b - a)}{D_c}. \quad (8)$$

276 This implies that quasi-static steady-state slip is stable ($V \rightarrow V^*$) or unstable ($V \rightarrow \infty$)
 277 if the spring stiffness is greater than or less than the critical value k_{cr} , respectively. Fault
 278 stiffness is inversely proportional to the minimum half-length of a nucleation zone capable
 279 of instability:

$$L_c = \eta \frac{G^* D_c}{\sigma_n (b - a)}, \quad (9)$$

280 where $\eta = (7\sqrt{2})/(3\pi)$ (Dieterich, 1992) for a square patch, the corrected shear modulus
 281 $G^* (= G/(1 - \nu))$ was employed due to the Mode II plane strain conditions and ν is the
 282 Poisson's ratio.

283 The equation of motion controlling slip on a planar fault is given by:

$$\tau_{el}(\mathbf{x}) - \tau(\mathbf{x}) = \frac{G^*}{2V_S} V(\mathbf{x}), \quad (10)$$

284 where τ_{el} is the elastostatic shear stress due to the loading boundary condition (Horowitz
 285 & Ruina, 1989). The inertial term on the right hand side represents the radiation damping
 286 term for S waves produced along the fault at point \mathbf{x} , which expands at speeds closer to the
 287 shear wave speed V_S of the material (Rice, 1993).

288 Quasi-static interactions between fault elements are calculated using the boundary ele-
 289 ment method (BEM) and all calculations reported in this study were solved using a Quasi-
 290 DYNAMIC earthquake simulator (Luo et al., 2017). QDYN is a boundary element software
 291 designed to simulate earthquake cycles (seismic and aseismic slip on tectonic faults) under
 292 the quasi-dynamic approximation (quasi-static elasticity combined with radiation damping)
 293 on faults governed by RSF and embedded in elastic media. Solution convergence and mesh
 294 discretization of the heterogeneous models described later is given in Supplemental Methods
 295 S1.

296 Dieterich (1992) showed that RSF combined with elasticity leads to the common length
 297 scale

$$L_b \equiv \frac{G^* D_c}{\sigma b}. \quad (11)$$

298 This characteristic dimension was later theoretically confirmed by Rubin and Ampuero
 299 (2005) and controls aspects of earthquake nucleation and the transition from aseismic to
 300 seismic behaviour. We define this transition threshold to be:

$$V_{dyn} = \frac{2aV_s}{G^*}, \quad (12)$$

301 which represents the transition point where the inertial term in equation eq8a becomes
 302 significant.

303 **2.2 Recent advances in RSF modeling from the laboratory**

304 Experiments performed by Nielsen et al. (2010) and Latour et al. (2013) have benefited
 305 from increasing the fault’s compliance using analog materials (glassy polymers) in frictional
 306 tests. These experiments benefit from improved spatio-temporal measurement of slip was
 307 achieved by using high speed digital cameras. Increased refinement in both spatial and
 308 temporal measurements clearly showed the so-called “preslip” or nucleation zone. This
 309 nucleation region was predicted in RS models (Dieterich, 1992; Rubin & Ampuero, 2005;
 310 Ampuero & Rubin, 2008) but was difficult to show with high spatial resolution before novel
 311 sensing techniques.

312 Modeling efforts by Kaneko and Ampuero (2011) and Kaneko et al. (2016) showed that
 313 frictional behavior of the ‘plastic-on-plastic’ sliding experiments can be explained using RS
 314 friction models. These models are informative and promote the idea of a ‘smooth transition’
 315 of frictional sliding over the macroscopic length scale of the experimental fault. It explained
 316 both the spatial and temporal evolution of observed nucleation features of those laboratory
 317 ruptures. While these studies have demonstrated RSF ability to explain complex transients,
 318 neither addressed the role of fault roughness; they assumed this is embedded implicitly in
 319 the phenomenological nature of the RSF parameters.

320 Roughness has been established to affect dynamic rupture propagation (e.g. Dunham
 321 et al., 2011; Fang & Dunham, 2013), nucleation physics (e.g. Tal et al., 2018) and the
 322 presence of aseismic transients (Ozawa et al., 2019). In these studies the fault is considered
 323 to be perfectly mated and roughness is described using the Hurst exponent. As the level
 324 of fault matedness in the modeled experiments was unclear at any time, we chose to use a
 325 *cutting plane method* that spatially discretizes the frictional properties applied on a planar
 326 fault by using measurements inferred from the two (smooth and rough) surfaces defined by
 327 bimodal Gaussian model described before.

328 2.3 Cutting plane method

329 The *cutting plane method* splits the roughness into two separate sections: smooth and
 330 rough. Using this method we assign binary sets of frictional parameters to both the smooth
 331 and rough regions of the roughness profile. A ‘cutting plane’ was defined to be exactly
 332 between the two means of the bimodal distributions that was formed due to wear. In this
 333 study, we build a simple 1-D model and arbitrarily choose the transect of the rough surface
 334 at $y = 2$ mm. Figure 3(a) displays the roughness along x at $y = 2$ mm (black line). In
 335 Figure 3(a), (b) and (c) the cutting plane (red) was defined as $h_{cut} = (\mu_1^* + \mu_2^*)/2 = 12.54$
 336 μm using the bimodal Gaussian parameters calculated for surface heights along transect
 337 at $y = 2$ mm. Figure 3(b) depicts the probability distribution of the surface heights from
 338 the sample transect and the cutting plane in red. We assume that the “smooth” surface
 339 is the “upper” one (above the cutting plane) that is characterized more effectively by the
 340 Gaussian distribution with lower standard deviation (σ^*), whereas the “rough” surface was
 341 below the cutting plane and had a larger standard deviation.

342 A scaling function (SF) is used to partition the smooth and rough sections of the fault.
 343 Figure 3(c) marks a detailed view of the roughness (black), the cutting plane (red) and the
 344 scaling function (blue). When roughness was above the cutting plane the scaling function
 345 (SF) was unity. All heights below the cutting plane were prescribed as scaled values. This
 346 allowed us to control the magnitude, or ‘order’, of heterogeneity. For this example, the
 347 order was $O = 20$. The SF produced heterogeneity in two ways: (i) spatial variations were
 348 controlled by the location where the roughness profile crossed the cutting plane, and (ii) the
 349 level (order) of heterogeneity – the peak-to-peak range of SF – was chosen by the modeler.
 350 The order of the $SF(x)$ is clearly seen in the PDF in Figure 3(d).

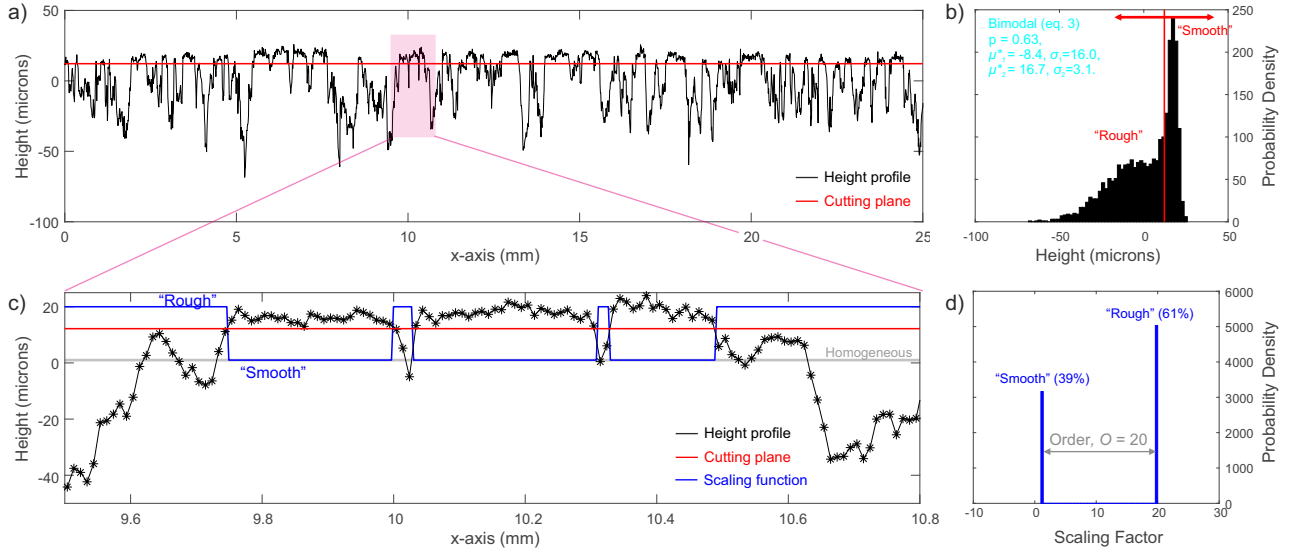


Figure 3. (a) 1-D roughness profile (black) taken from the transect at $y = 2$ mm in Figure 1(f). The cutting plane $h_{cut} = 12.54 \mu\text{m}$ is used to separate the bimodal distribution into smooth and rough surfaces. (b) PDF of the height profile in (a) with the cutting plane (red vertical line). (c) Small section of the height distribution showing the roughness profile (black line), the cutting plane (red line) and the scaling function (blue line). (d) PDF of the scaling function $SF(x)$ with an order of heterogeneity $O = 20$.

351 We approach the modeling in a non-traditional manner and imposed heterogeneity pri-
 352 marily through the frictional critical slip-weakening variable $D_c(x)$. Spatial fluctuations
 353 in fault roughness – smoother and or rougher sections – assumed properties based on argu-
 354 ments in past laboratory observations (Marone & Cox, 1994). This assumption also
 355 follows micro-mechanical simulations governing the critical slip-weakening variable D_c on
 356 dry, gouge-free interfaces (Yoshioka & Iwasa, 1996; Yoshioka, 1997). Smooth sections were
 357 prescribed lower $D_{c,low}$, whereas rougher sections have a higher level of $D_{c,high}$. Spatial
 358 fluctuations in critical slip distance was given the lower value multiplied by the scaling func-
 359 tion $D_c(x) = D_{c,low} \cdot SF(x)$. The magnitude D_c in the rough sections depended on the order
 360 O of the scaling function. For example, for order $O=20$, the larger critical slip value was
 361 $D_{c,high} = \max[D_c(x)] = 25 \text{ nm} \cdot 20 = 500 \text{ nm} = 0.5 \mu\text{m}$.

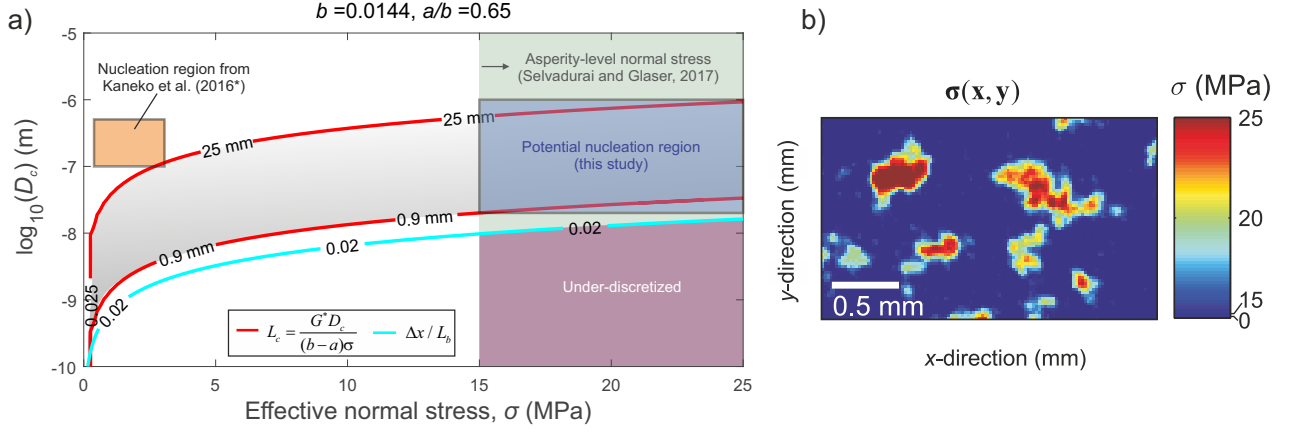


Figure 4. (a) Initial estimates of the nucleation parameter space (L_c) based on measurements of local normal stress (Selvadurai & Glaser, 2017), minimum mesh discretization ($\Delta x/L_b$) and maximum critical nucleation size $L_c = 0.025$ m. The gray region represents possible nucleation sizes for the mesoscopic length scale. The orange region represents the ranges of D_c and normal stress σ_n that nucleated full fault rupture in ? (?), $a/b = 0.6944$ Kaneko2016. (b) Example of asperity-level normal stress field measured using an experimental pressure sensitive film (adapted from Selvadurai & Glaser, 2017).

2.4 Frictional parameter space

Although we chose parameters based on our previous studies we also incorporated assumptions from the literature. The goal of our modelling is to identify conditions that produce local seismicity – a critical experimental observation obtained from the PZT sensors. Figure 4 demonstrates how the critical nucleation length L_c (equation eq8) varies with D_c and the normal stress σ_n . Based on experiments performed by Berthoude et al. (1999) for PMMA, we set $a/b = 0.65$ and $b = 0.0144$. For reference, curves representing constant critical nucleation length are marked in red for $L_c = 25$ mm and 0.9 mm.

To further constrain our models, we examined the experimentally measured asperity normal stress from the concerted study of Selvadurai and Glaser (2017). Using the calibrated pressure film (Selvadurai & Glaser, 2015b), they found the asperities attained normal stresses ranging from $\sigma_n = 12$ to 25 MPa. This range of normal stress is superimposed in Figure 4(a), which further bounds the potential nucleation conditions in our RSF model.

Adequate fault meshing for the numerical simulations is needed to correctly capture the dynamic processes at the rupture tip during seismic events. Our calculations were

377 based on estimates of the cohesive (or breakdown) zone length scale L_b (equation eq8b).
 378 We found that to accurately capture local frictional breakdown it was necessary to apply
 379 a minimum grid size of $\Delta x/L_b < (1/50)$ was needed for $a/b = 0.65$. In this model we
 380 choose to use $2^{13} = 8192$ grid points over the length $L = 25$ mm of the mesoscopic domain,
 381 resulting in a resolution $\Delta x \sim 3 \mu\text{m}$. Our domain is much smaller than previous RSF
 382 model used to understand laboratory friction experiments. The macroscopic parameter
 383 space used by Kaneko et al. (2016) (orange region) to understand the behavior of similar
 384 plastic-on-plastic sliding experiment performed by Latour et al. (2013) is given for reference.
 385 Table 1 presents baseline frictional, material and length scale parameters used in this study.
 386 More information on the convergence tests for the heterogeneous models is given in the
 387 Supplemental Information S1.

Table 1. General model parameters used in the 1-D RSF models.

Parameter	Symbol	Value
Shear modulus	G	2.39 GPa
Poisson ratio	ν	0.32
Shear wave speed	V_S	1330 m s ⁻¹
Reference friction coefficient	μ	0.6
Reference slip rate	V^*	0.1 $\mu\text{m s}^{-1}$
Dynamic sliding threshold	V_{dyn}	0.177 m s ⁻¹
Loading plate velocity	V_{LP}	0.1 $\mu\text{m s}^{-1}$
Lower critical slip distance	$(D_c)_{low}$	25 nm
Heterogeneous critical slip distance	$D_c(x)$	$(D_c)_{low} \cdot \text{SF}(x)$
Normal stress	σ_n	25 MPa
Length of mesoscopic domain	L	25 mm
Height of mesoscopic domain	H'	2.5 mm
Width of mesoscopic domain	W	∞
Grid size	Δx	3 μm
Grid points	n	2^{13}
RS parameter b (VW)	b	0.0144
RS parameter a (VW)	a	0.00936
Simulation time	t_{sim}	600 s

3 Computational Results

The general domain for our 1-D frictional model is presented in Figure 5(a). This represents the mesoscopic region under the eddy current target in Figure 1(c). The geometry of the domain is $L = 25$ mm (extent of the roughness measurement in the direction of slip), $H' = 2.5$ mm (height of the material just below the eddy current target) and $W = \infty$ (plane strain conditions). The boundary element code QDYN assumes frictional properties (a , b and D_c) and normal stress (σ_n) at each node on the interface. Figure 5(b) displays a schematic representation of the boundary value problem. A few representative nodes are depicted as slider blocks. Communication between frictional nodes is shown as spring elements. QDYN solves the equation of motion given in eq8a. Before moving to more complex, heterogeneous cases we examine the behavior of the homogeneous case to develop the fundamental understanding of the system and to establish the reference case.

3.1 Homogeneous case

From the mesoscopic geometry we build the 1-D homogeneous model, expressed schematically in Figure 5(b). For the homogeneous case, each node has velocity-weakening (VW) conditions $(a - b) = -0.005$, $a/b = 0.65$, normal stress $\sigma_n = 25$ MPa and a critical slip-weakening distance $D_c = 25$ nm. For the homogeneous case, the steady-state sliding velocity V^* was assumed to be equal to the load point velocity V_{LP} . We were able to determine this experimentally from the near-fault slip velocity measurements made using the eddy current slip sensors displayed in Figure 1(d); $V_{LP} = 0.1 \mu\text{m/s}$ was used in this study.

Each numerical simulation lasted for $t_{sim} = 600$ s, which allowed the fault to fully-develop a periodic stick-slip response (Hillers et al., 2007). Figure 5(c) and (d) show a short time window (500 to 600 s) of the slip velocity and shear stress, respectively, averaged over all nodes in the model. We see that periodic ruptures are analogous to a ‘stick-slip’ event. Over the full simulation, 18 full rupture stick-slip events were recorded for the homogeneous case but only three are displayed here. Coseismic slip was defined when any node experienced a sliding velocity $V > V_{dyn} = 0.177$ m/s defined by equation eq8c. To further characterize the homogeneous case, Figure 5(e) reveals the relationship between average slip velocity and shear stress, which depicts the seismogenic evolution of the systems between different seismic regimes: interseismic, preseismic, coseismic and postseismic (Ampuero & Rubin, 2008).

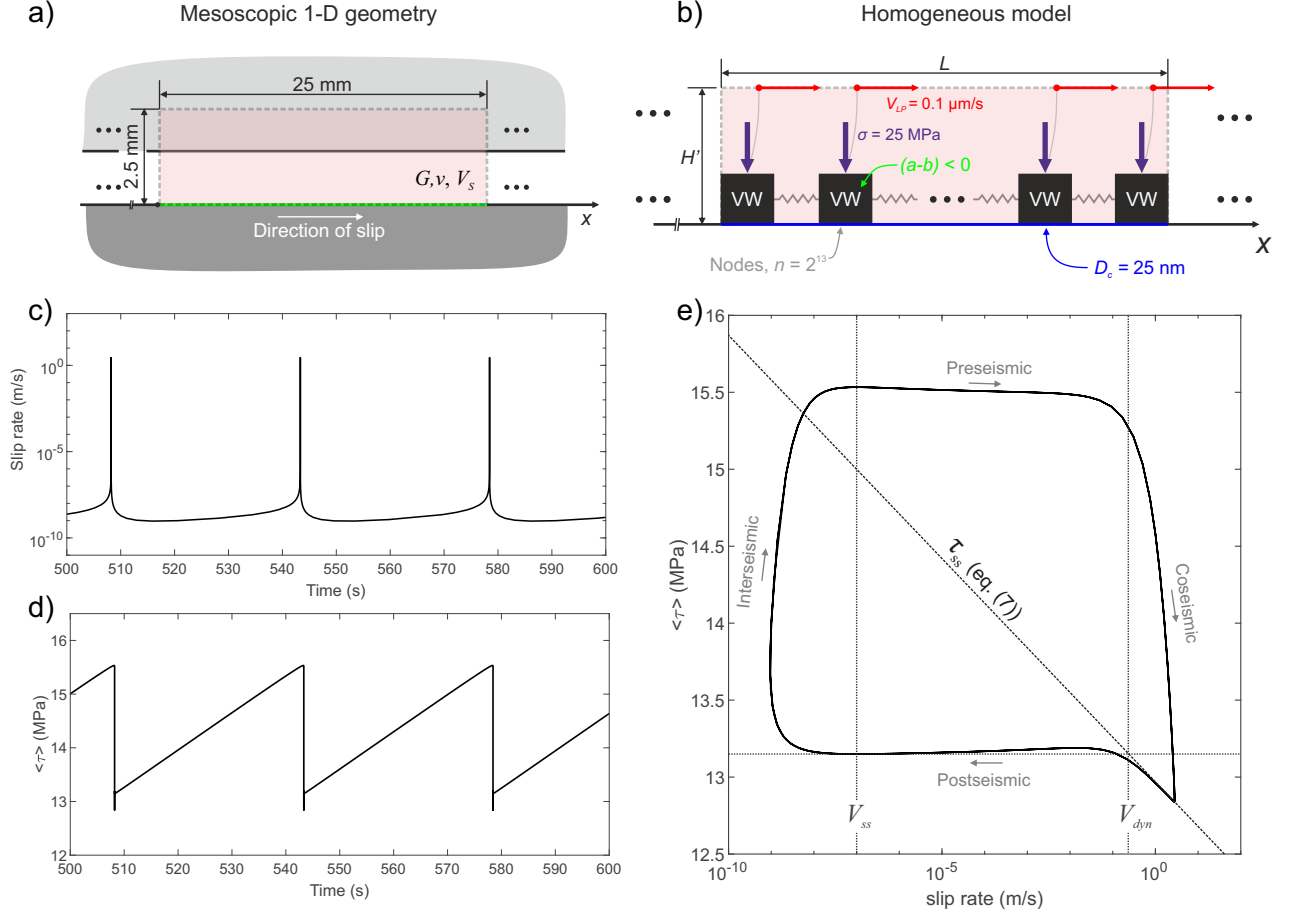


Figure 5. (a) General dimensions of the model domain in Figure 1(c). (b) Description of the 1-D boundary value problem being solved by QDYN. RS frictional behavior is described by equations eq5 to eq8. (c) Average slip velocity and (d) average shear stress along the fault for t_{sim} between 500 to 600s. We see that the fault underwent stick-slip behavior. (e) A diagram of the earthquake cycle for the VW fault that includes preseismic, coseismic, postseismic and interseismic phases.

3.2 Heterogeneous D_c -model

We produce heterogeneity by varying the distribution of the critical slip weakening distance D_c according to the scaling function (SF) in Figure 3(c). The D_c -model shares some properties of the homogeneous case ($b = 0.0144$, $a/b = 0.65$, $\sigma_n = 25$ MPa) and is depicted schematically in Figure 6(a). For the D_c -model we prescribe the lower value of critical slip weakening distance $D_{c,low} = 25$ nm. Using the scaling function from the cutting plane method, we can capture the spatial variation in the critical slip weakening distance given as $D_c(x) = D_{c,low} \cdot \text{SF}(x)$. Figure 6(b) reveals the spatial fluctuations in $D_c(x)$ for heterogeneity on the order of O20. For reference, the spatial distribution of the homogeneous properties are given in Figure 6(c).

The average slip rate and shear stress for this D_c -model (O20) are marked in blue in Figures 6(d) and (e), respectively. For reference, we also depict the results from the homogeneous model O1 (black). We see that the fault experienced stick-slip behavior – the small spikes in slip velocity – but did not experience full rupture with a large drop in shear stress drop as in the homogeneous case.

Next we investigated the effect of different levels of heterogeneity. In Figure 7 the average fault behavior is depicted for three levels, O10 (red), O15 (green) and O20 (blue), that all use the same scaling function $\text{SF}(x)$. This is compared to the average behavior of the homogeneous fault O1 (black). The average slip, slip rate and shear stress are given in Figures 7(a), (b) and (c), respectively. We observed an increase in complexity from homogeneity with these models; both O10 (red) and O15 (green) still experienced full system-wide rupture (large events that propagated over the full extent of the modeled fault). Full rupture nucleated from a smooth section of the fault and did not always arrest when compared to more localized ruptures that occurred in the O20, which had stronger barriers.

We see that, along with system-wide events, O10 (red) and O15 (green) also experienced small localized events that were arrested by neighbouring barriers. We defined these as “foreshock sequences” (discussed later in more detail) leading up to the mesoscopic main rupture (larger stress drop on system-wide events), highlighted in Figure 7(c). We see that as the order O is increased, the fault exhibits transition from well-behaved (homogeneous, O1) to visibly disordered system with full ruptures mixed with small localised ruptures (O10 and O15), then returning to well-behaved, creep-dominated faults with only small localized events on a preferential patch (O20).

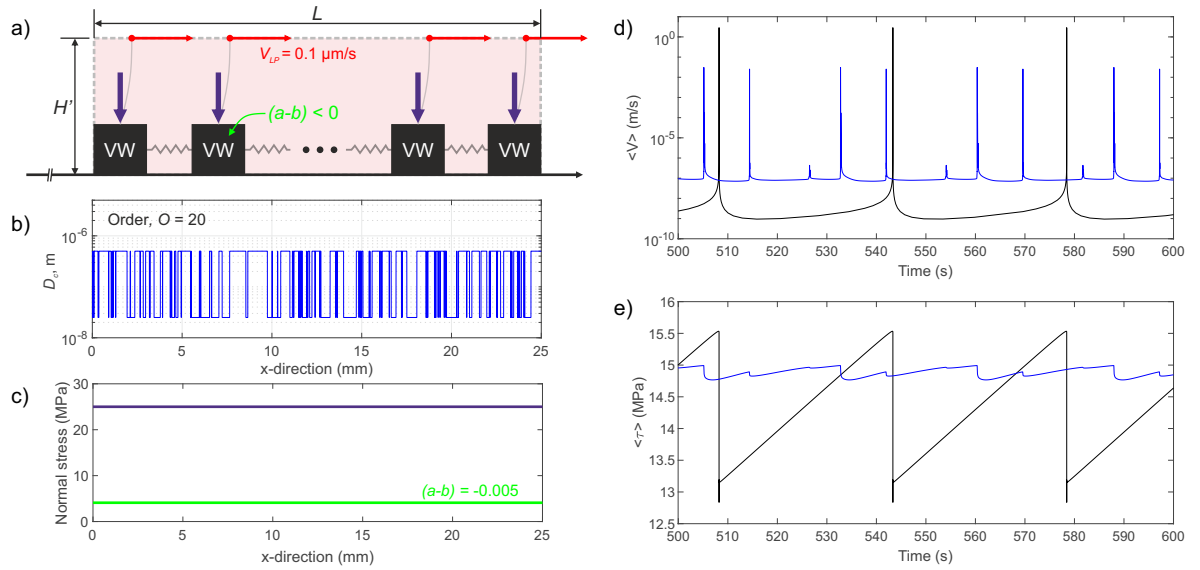


Figure 6. (a) General schematic showing the heterogeneous model. (b) Heterogeneous distribution of D_c , with $O=20$. (c) Constant normal stress and VW rheology ($a - b < 0$) is shown along the x -axis. (d) Average slip velocity is given along the fault for the heterogeneous model (blue line), which is compared to the homogeneous model (black line). (e) Average shear stress along the fault for the heterogeneous model (blue line), which is compared to the homogeneous model (black line).

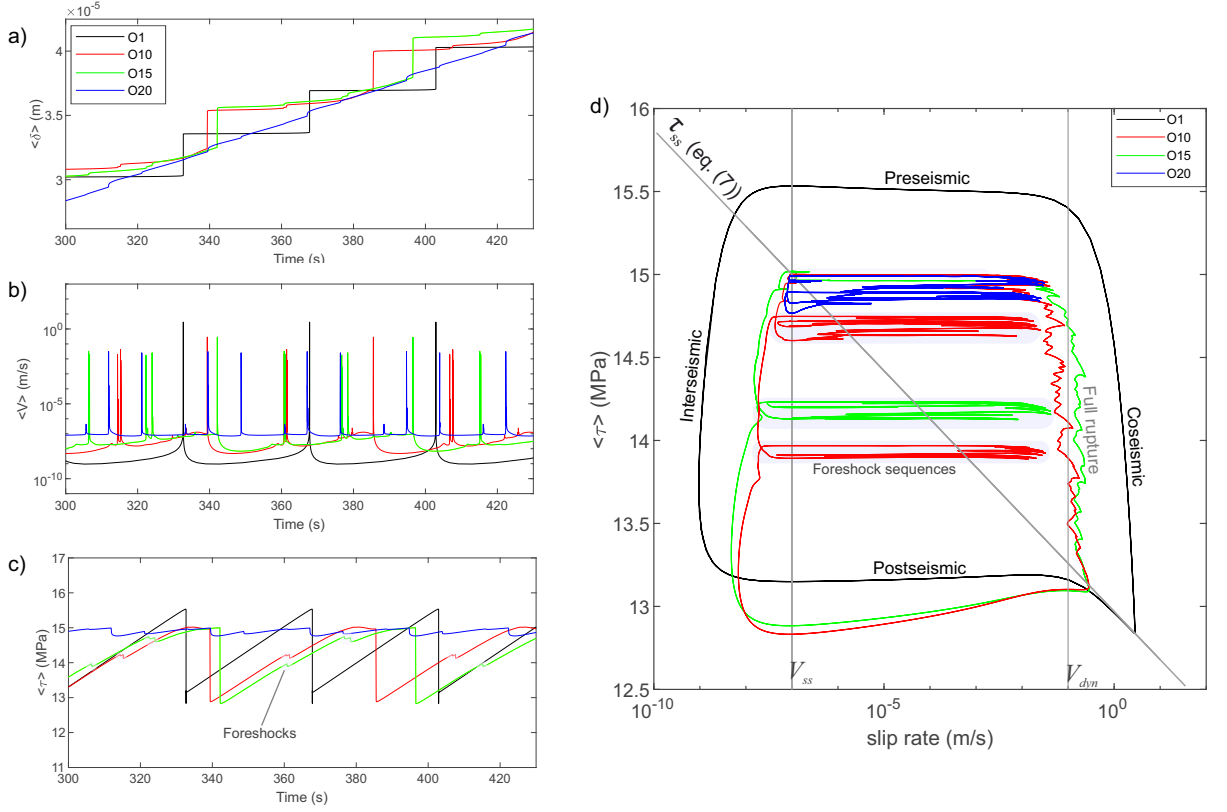


Figure 7. Three heterogeneous models $O = 10$ (red), 15 (green) and 20 (blue) are compared to the homogeneous model (black) for a short time window between 300 and 430 s. We show the (a) average slip, (b) average slip velocity and (c) average shear stress. We highlight where small drops in shear stress were seen and relate them to small localized events (foreshocks). (d) We examine the phase diagram between shear stress and slip velocity for each heterogeneous model compared to the homogeneous model.

451 To better visualize the system’s behavior, we plot all models on phase-diagrams de-
 452 scribed in Figure 7(d) for all cases to compare to the homogeneous system response. The
 453 average cycles from co- to post- to inter- to pre-seismic behavior, moving around τ_{ss} in
 454 equation eq7. The O10 (red) and O15 (green) models appear to show, in general, lower
 455 total stress drops during full rupture events compared to the homogeneous case. We also
 456 see that during a full rupture, the average slip rate on these faults is generally lower than
 457 in the homogeneous case. For the most heterogeneous fault with the order O20, full rup-
 458 ture events did not occur but there was some deviation from steady state caused by small
 459 foreshock sequences that prevented the fault from simply ‘creeping’ along at a constant slip
 460 rate and steady state shear stress.

461 These foreshock sequences are highlighted in phase diagram (gray regions) (Figure
 462 7(d)). Two major sequences were observed for the O10 and O15 models. The timing of
 463 these foreshock sequences, relative to the full fault cycle, are presented for O10(red) and
 464 occurred in the interseismic stages of the main rupture cycle. For O15(green), one foreshock
 465 sequence occurred in the interseismic portion and one occurred soon after the fault entered
 466 the nucleation phase of the larger rupture cycle. For O20 (blue), this smooth section of the
 467 fault prone to localized rupture behaved in a relative synchronous manner. More details to
 468 the spatio-temporal complexity of these ruptures are given in the next section.

469 *3.2.1 Spatio-temporal behavior or precursory seismicity*

470 In Figure 8 we examine the spatio-temporal evolution of the D_c -model with O17.5.
 471 This model was not presented in the previous section. The purpose of the previous section
 472 was to highlight changes in the general fault behavior at three levels of heterogeneity with
 473 distinctly different character. All spatio-temporal distributions of slip are depicted in a
 474 similar manner to Figure 8 in Supplemental Sections S3 for all models.

475 Figure 8(a) displays the spatio-temporal evolution of slip along the fault from time
 476 $t = 300$ s to 600 s. The time step between each isochron was uniform, taken every 30
 477 intervals of adaptive time steps. We note that if any point on the fault slipped rapidly,
 478 the adaptive time step would decrease to accurately solve the boundary value problem.
 479 Seismicity (red slip isochrones) was defined as any node in the model experiencing slip
 480 velocities $V > V_{dyn} = 0.177$ m/s. Below this threshold the fault was assumed to slide

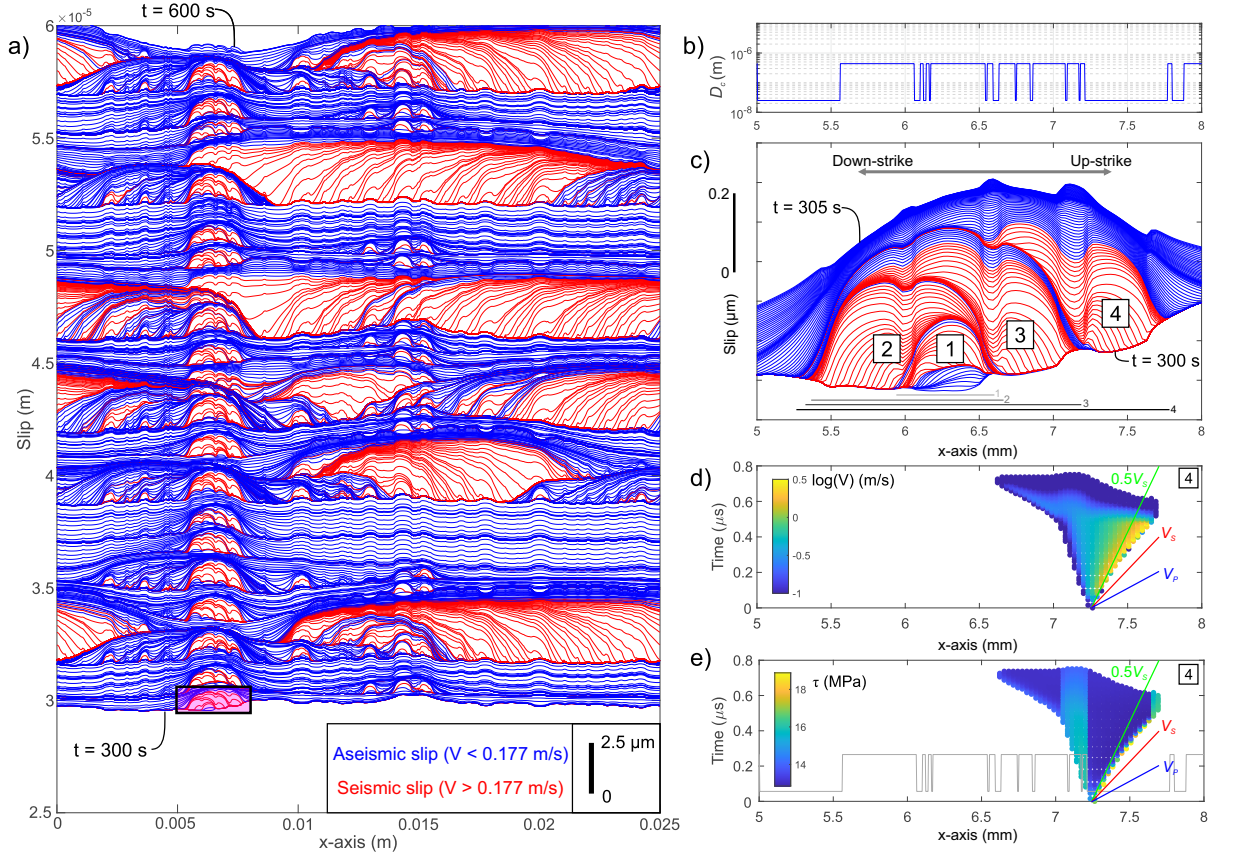


Figure 8. (a) Complex rupture for a fault with heterogeneity order $O = 17.5$. Slip along the fault are given for individual isochrones when the fault was sliding seismically (red, $V_{dyn} > 0.177$ m/s) or aseismically (blue, $V < 0.1$ m/s). Results only present simulation times between $t = 300$ s and 600 s. We use these results to calculate the properties of the localized ruptures that showed local nucleation, dynamic rupture and arrest behavior due to heterogeneity in D_c . (b) Spatial heterogeneity for a dominant asperity of the fault from $x = 5$ to 8 mm. (c) A small sequence composed of four individual ruptures between time $t = 300$ s to 305 s on the dominant asperity. The rupture demonstrates complex distributions of slip and spatio-temporal distributions. To better understand the temporal changes of the rupture, we show the spatio-temporal evolution of Event 4 in terms of its (d) slip velocity and (e) shear stress.

481 aseismically (blue slip isochrones). Using this description we clearly identify certain ‘seismic
482 patches’.

483 One patch is highlighted in Figure 8(a) and enhanced in (c) where we examine slip on
484 the transect $x = 5$ to 8 mm from $t = 300$ s to 305 s. This asperity section of the fault
485 was prone to seismicity in all models, even the O20 that showed limited localized seismicity
486 and we refer to this as *dominant asperity* from herein. Figure 8(b) demonstrates the spatial
487 variability in heterogeneity in D_c along that section (for this case with O17.5). In Figure
488 8(c), we see that the fault slips aseismically between ruptures, which delineates the seismicity
489 over these five seconds. Four individual ruptures are presented, which exhibited crack-like
490 behavior but remain complex throughout the simulation due to the spatial variability in D_c ,
491 the level of heterogeneity (O17.5) and the continuously evolving shear stress on the fault.

492 In Figures 8(d) and (e) we investigate the space-time plot of slip velocity and shear
493 stress, respectively, for Event 4 in the asperity failure sequence. The portion of the fault x
494 $= 5$ to 8 mm is highlighted and we have superimposed the heterogeneity from Figure 8(b)
495 for clarity. We see that Event 4 nucleates at the edge of a ‘smooth-rough’ boundary ($x \sim$
496 7.25 mm) depicted as the purple star. As the rupture expands, it propagates bi-laterally
497 at different rates. We have superimposed three lines of constant velocity $0.5 \cdot V_S$ (green),
498 V_S (red) and V_P (blue). Upon nucleation, the rupture propagates outward in a subsonic
499 manner, moving faster ($\sim 0.75 \cdot V_S$) “up-strike” into the smoother, less resistive section than
500 into the “down-strike”, the rougher and more resistive section ($\sim 0.45 \cdot V_S$). This behavior
501 represented typical rupture behavior for localized events on the dominant asperity.

502 The spatio-temporal rupture evolution for Event 4 is enlarged in Figure 9(d). Subsonic
503 rupture propagation grows bi-laterally at different rates until arriving at separate barriers.
504 Once the up-strike crack-tip (i.e. that moving on the smooth fault) reached an up-strike
505 barrier, it was abruptly arrested (red star). As this rupture is arrested a back propagating
506 front is emitted moving closer to the P wave velocity; this front is known as the P stopping
507 phase. This stopping phase was observed by Madariaga (1976) in numerical simulations
508 of kinematic rupture on a circular asperity. In that problem, the P stopping phase is the
509 wave radiated when the rupture front suddenly halts (red stars), for example when it
510 encounters a strong enough barrier. Both the up- and down-strike rupture encountered
511 barriers and produced separate P stopping phases. For the down-strike propagating crack-

tip, this P stopping phase actually caused the overall dimension of the rupture to grow larger, eventually terminating at the green star.

To estimate the properties of each rupture we used an image detection algorithm (Gonzalez et al., 2009) and examined the 2-D distance-time space. Using the slip velocity threshold of $V_{dyn} > 0.177$ m/s, the ruptures were easily separated and the half-length L_r is displayed in Figures 9(d).

3.2.2 Constitutive behavior of individual ruptures

One goal of this study is to characterize, compare and validate our RSF model using source properties to those reported by Selvadurai (2019). We developed tools to quantify the cumulative slip (δ), static stress drop ($\Delta\sigma$), fracture energy (G') and rupture half-length (L_r) for each rupture to account for their individual complex behavior. In Figure 9 we look at the complex behavior of Event 4 from the previous section. Figure 9(d) reveals an enlarged view of Event 4 that ruptured a section with 1-D rupture dimension $2L_r$. To better understand the complex behavior of all seismic ruptures moving forward, we divide the full length of the rupture into 25 equally-spaced points along the x -axis. The number of transects used was sufficient to sample ruptures and to conduct a sensitivity study that investigated the number of required sampling transects (Supplementary Section S2).

Figure 9 provides a concise temporal understanding of the diversity in the temporal evolution of: (a) slip, (b) slip-rate and (c) shear stress along the spatial transects of Event 4. In Figure 9(a) the rupture has a non-uniform distribution of accumulated slip. The average slip along the 25 estimates was $\delta = 0.37$ μm . We use this to estimate the scalar seismic moment M_0 given by Aki (1966):

$$M_0 = GA\delta, \quad (13)$$

where A is fault area and δ is slip. For a penny-shaped fault $A = \pi r^2$ and for a square fault $A = (2L_r)^2$. Using this estimate the scalar seismic moment $M_0 = 0.0014$ N·m. This is equivalent to a moment magnitude $M_w = -7.94$. Transects were color coded for the smooth (red) and rough (black) sections of the fault to highlight differences in dynamic response. As expected, rougher sections showed higher variability in cumulative slip along each transect since they were responsible for arresting the rupture.

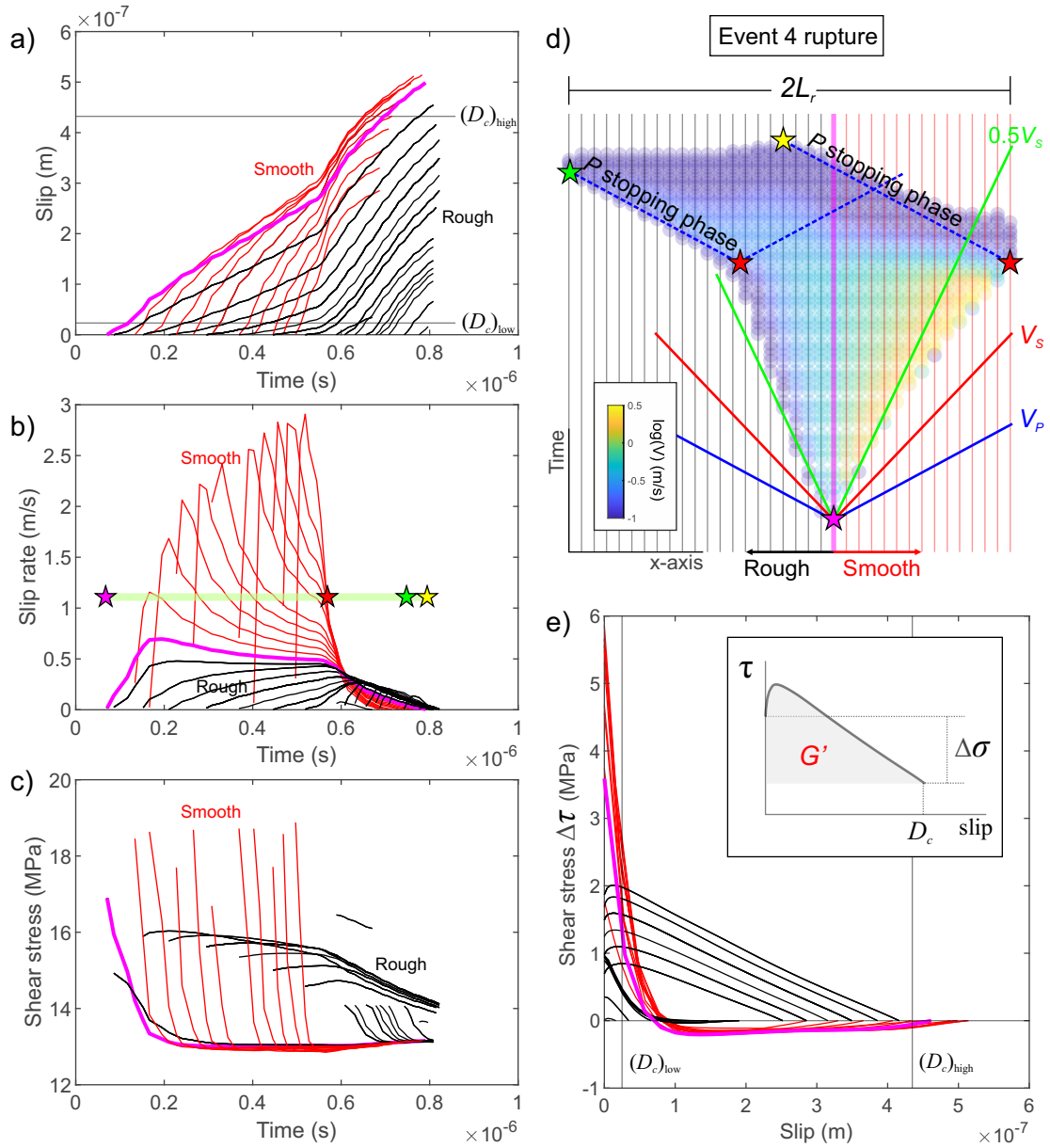


Figure 9. Rupture complexity of Event 4 in Figure 8(d) and (e) in space-time plots. (a) Temporal evolution of slip along 25 different transects of rupture spaced evenly on the fault. (b) Temporal evolution of slip rate along the transects in (a). Key instances of rupture are marked by the colored stars. (c) Temporal evolution of shear stress for the same positions as in (a). (d) Space-time plot of the rupture with the transects depicted graphically. (e) The traction-slip from each transect; the inset image depicts measurements of (static) stress drop ($\Delta\sigma$) and fracture energy (G') for each position on the fault.

540 The slip rate along each transect is displayed in Figure 9(b). For further clarity, im-
 541 portant times of the rupture are marked by superimposed colored stars. The rupture has
 542 higher slip rates along the smoother section of the fault, whereas the rough section offers
 543 more resistance with lower slip rates. Shear stress along each transect is presented in Fig-
 544 ure 9(c). Smooth portions of the fault (red lines) achieve higher peak stress and exhibit
 545 higher weakening rates than the rough sections (black lines), which offer higher resistance
 546 to rupture.

547 Figure 9(e) demonstrates the slip-traction relationship for each transect. Values are
 548 normalized with regards to the final stress. Using the inset image we can estimate the
 549 (static) stress drop ($\Delta\sigma$) and fracture energy (G'). The latter is sometimes referred to as
 550 breakdown work defined by the area under the slip-traction curve (e.g., Tinti et al., 2005;
 551 Cocco et al., 2016). We find substantial differences in the participation of each surface
 552 (rough and smooth) in the metrics that have been extracted.

553 For clarity we have highlighted the critical slip weakening distance for both the smooth
 554 $D_{c,low}$ and rough section of the fault $D_{c,high}$. We see that in some cases slip was greater than
 555 $D_{c,high}$, which may be explained as dynamic overshoot (Madariaga, 1976). Calculating $\Delta\sigma$
 556 is relatively straightforward; to determine the fracture energy G' , we numerically integrated
 557 the area under this curve. For Event 4, the average static stress drop was $\Delta\sigma = 3.25$ MPa
 558 and average fracture energy $G' = 0.13$ J/m².

559 3.3 Summary of precursory source properties

560 3.3.1 Seismic moment versus source size

561 In Figure 10(a) we examine the relationship between source area $A_r = (2 \cdot L_r)^2$ and
 562 seismic moment M_0 for the different RSF models. Source properties determined in the
 563 previous section are compared to those inferred from seismic waves from an in-depth study
 564 by Selvadurai (2019). We show the results five D_c -models (circles) against the kinematic
 565 estimates detailed by Selvadurai (2019) from P and S waves (triangles). Full ruptures
 566 referred to events that ruptured the entire fault surface. RSF ruptures followed the classical
 567 empirical scaling relationship between seismic moment and source geometry ($M_0 \propto L_r^3$).
 568 Figure 10(c) displays the relationship between stress drop and seismic moment, which was
 569 relatively constant ~ 1.86 MPa where smaller ruptures had slightly lower values of stress
 570 drop.

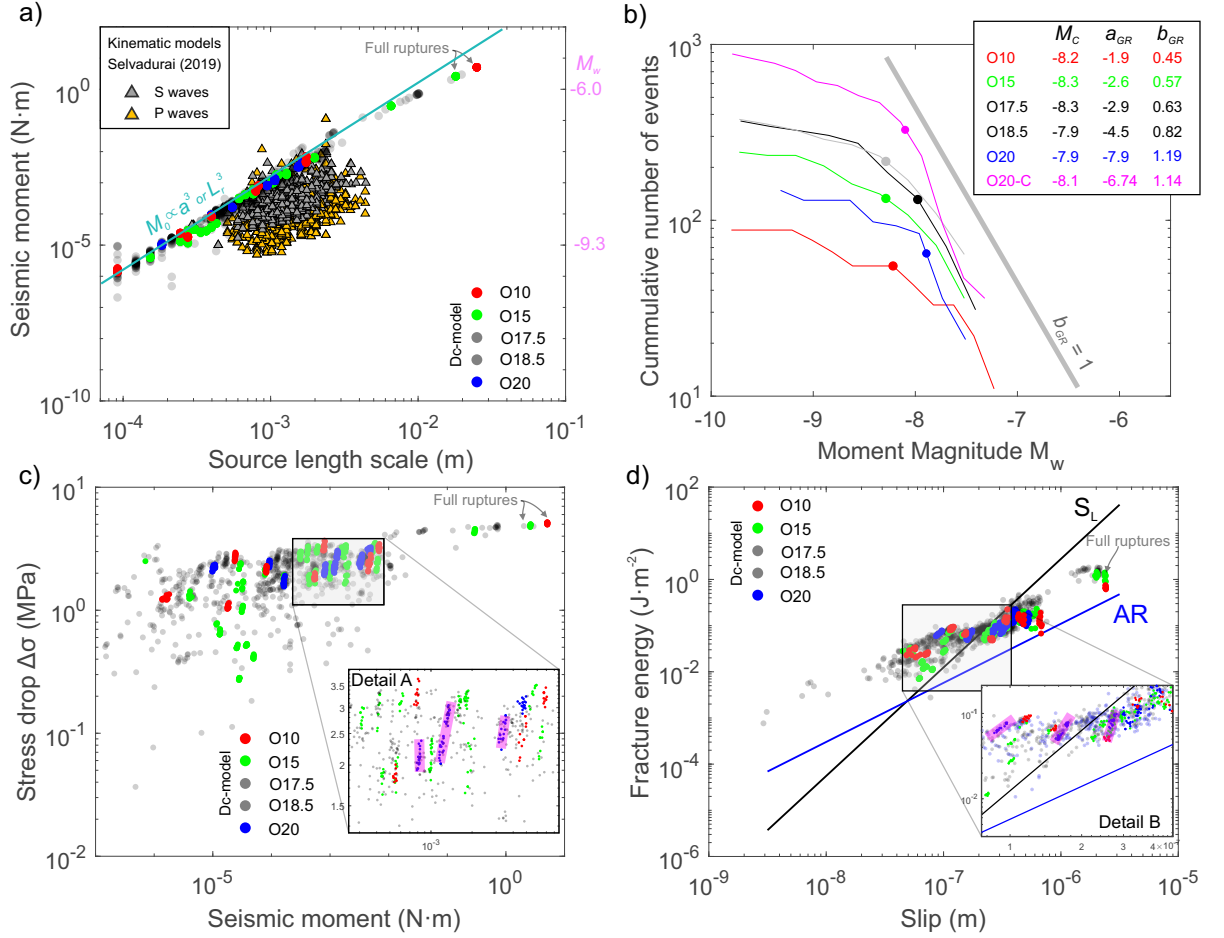


Figure 10. (a) Source length calculated from the numerical models with various levels of heterogeneity (colored circles) compared to their scalar seismic moment M_0 . These are compared to the kinematic estimate of source properties determined using shear crack models Selvadurai (2019) for both P and S waves (triangles). (b) Frequency-magnitude distributions (FMDs) are given for each model catalog with $b_{GR} = 1$ depicted as reference. The inset legend gives the GR parameters: a_{GR} , b_{GR} and the magnitude of completeness M_c . (c) Relationship between stress drop ($\Delta\tau$) and ruptured area M_0 . (d) Fracture energy (G') versus slip. We compare the models to empirical scaling estimates from laboratory seismicity (black line, Selvadurai, 2019) and extrapolated field estimates (blue line Abercrombie & Rice, 2005).

3.3.2 Frequency-magnitude distribution

Estimates of the frequency-magnitude distributions (FMDs) are shown in Figure 10(b). The Gutenberg-Richter (GR) law describes the magnitude distributions of earthquakes following the standard relationship $\log_{10}(N) = a_{GR} - b_{GR}M_w$, where N is the number of events equal to or above magnitude M_w and a_{GR} and b_{GR} are constants describing the productivity and sizes of earthquakes, respectively (e.g. Wiemer & Wyss, 2002).

The legend gives the maximum likelihood estimate of the a_{GR} - and b_{GR} -values computed based on events above the magnitude of complete recording M_c (Wiemer & Wyss, 2002). Typically M_c is used to assess the completeness of the catalog under investigation, i.e. above which magnitude does the GR law fits the data best. We note that the nature of the GR relationship is scale-invariant and in our model, where all events can be recorded without converge bias, the completeness magnitude M_c is related to physical effect discussed later in Section 4.6. As the order of heterogeneity increases so do estimates of a_{GR} - and b_{GR} -values. Lower b_{GR} were observed on stick-slip dominant fault (O10 and O15) and increased on creeping faults (O20) which is discussed more thoroughly in Section 4.6.

3.3.3 Fracture energy scaling

Scaling behavior between fracture energy G' and slip δ is compared to the empirical relationship $G' \propto \delta^\gamma$. In Figure 10(d) estimates of G' for the different models are presented. These are compared to the previously discussed empirical relationship for shear crack source models from laboratory experiments (S_L , $\gamma = 2.35$) (Selvadurai, 2019) and estimates made at regional scales from natural earthquakes (AR, $\gamma = 1.28$) following the observations of Abercrombie and Rice (2005) (see also Mai et al., 2006). We see that the results from the model tend to follow the same slope as AR but, if we look more closely, at Detail B in Figure 10(d), we see that some of the smooth patches show steeper trends in scaling. This can be explained by the fact that the preferential worn patches remain relatively constant in size but the stress drop varies, as depicted in Detail A of Figure 10(c).

3.3.4 Creeping to stick-slip transition

Figure 11 marks the average slip (black) and average shear stress (red) for 100 s of the simulations for strong barriers O20 (left-hand side, LHS) to weaker barriers O10 (right-hand side, RHS) and the transitional case O17.5 (middle panel). The general behavior of the fault

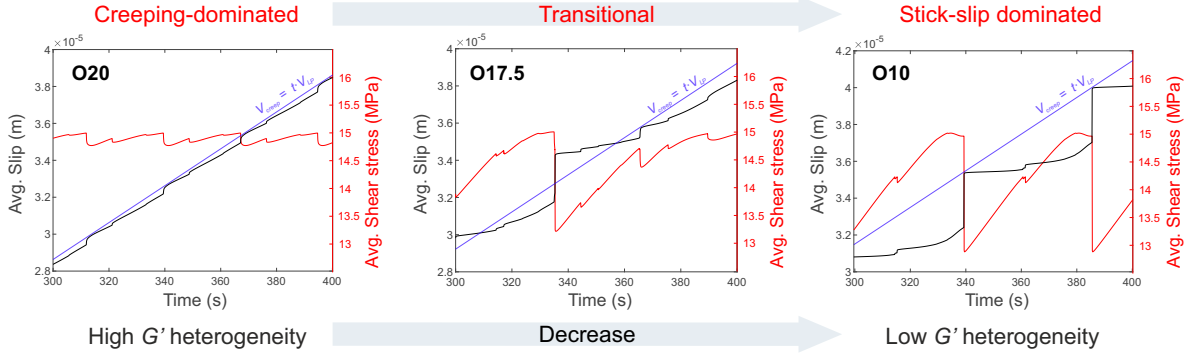


Figure 11. Earthquake recurrence rate for each D_c -model from higher O20 to lower O10 levels of strength heterogeneity. (a) The average behavior of the entire fault for small portions of time $t = 300$ to 400 s for the O20 (creeping-dominated), O17.5 (transitional) and O10 (stick-slip dominated) models.

601 transitioned from creep-dominated (O20) to stick-slip dominated (O10). Creep-dominated
 602 and stick-slip dominated are defined by how much the average slip deviates from the creep
 603 rate ($V_{creep} = t \cdot V_{LP}$). This transition from creep- to stick-slip-dominant behavior occurred
 604 as the level of heterogeneity was decreased. In all simulations, the fault was driven at a
 605 constant loading rate and its impact on the general behavior is the subject of future work.
 606 Figure 11 highlights the distinct regimes and the appearance of foreshocks in a broad sense
 607 (Mogi, 1963, 1985) are discussed in Sections 4.1 and 4.2.

608 3.4 Heterogeneous *Composite*-model

609 The primary goal of this study is to provide an understanding of what types of RSF
 610 heterogeneity may explain a suite of experimental observations. Prior models have employed
 611 heterogeneity with a minimal level of unknown variables. We increase the complexity of the
 612 model using a Composite-model; this model aims to illuminate any additional complexity
 613 that may exist in the spatial distribution of normal stress. This model is presented to expand
 614 the possible boundary conditions that can feasibly explain the concomitant slow and fast
 615 slip on a frictional interface.

616 We use measurements from the pressure sensitive film (Figure 4(b)) to implement vari-
 617 ability in normal stress. More information on the pressure sensitive film is given in Selvadurai
 618 and Glaser (2017). We use the scaling function where on smooth sections (low D_c) we pre-
 619 scribe constant normal stress $\sigma_{n,high} = 25$ MPa and on rough sections, we apply a constant

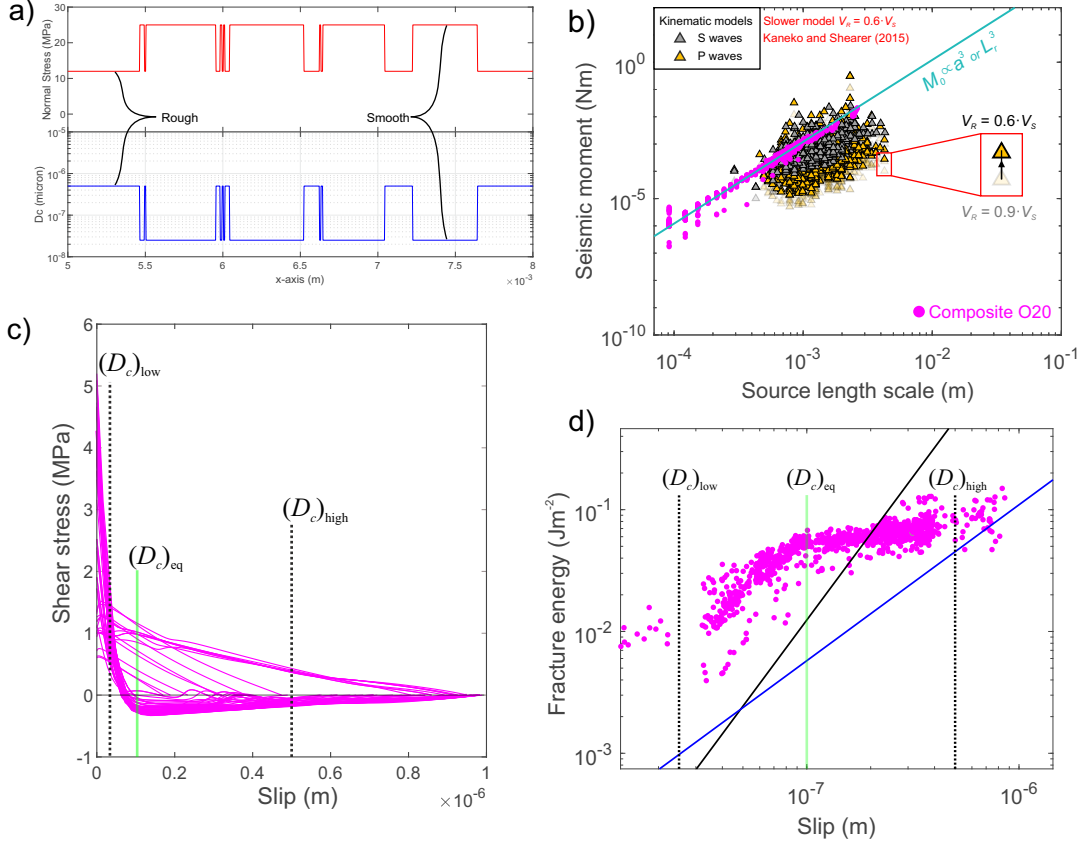


Figure 12. Results from the *Composite*-model. **(a)** A small section of the 1D fault from $x = 5$ to 8 mm showing the spatial variation in both D_c and σ_n . **(b)** The scaling relationship between A_r and M_0 (gray circles) is compared to the corrected kinematic estimates of source properties from Selvadurai (2019) (triangles). **(c)** Constitutive behavior for a large event in the *Composite*-model. **(d)** Relationship between fracture energy G' and slip δ . Empirical relationship between black and blue lines is similar to that demonstrated in Figure 10(d).

620 low normal stress level, set to the lower measurable limit of the pressure sensitive film $\sigma_{n,low}$
 621 = 12 MPa (Selvadurai & Glaser, 2015b).

622 Figure 12(a) depicts a section of the spatial heterogeneity on the dominant asperity
 623 under normal stress σ_n (red) and at a critical slip weakening distance D_c (blue). The
 624 scaling function was chosen to be O20, a model that previously had a relatively well-behaved
 625 response. We use the same methods to calculate source properties and examine similar
 626 relationships for this composite-model (O20C).

627 Figure 12(b) reveals the relationship between M_0 and A_r , with similar estimates as
 628 the kinematic shear crack model in Figure 10(a). However, here we have made additional
 629 assumptions in the shear crack model regarding rupture speed. We apply a correction factor
 630 to account for slower ruptures in kinematic models, for example $V_r = 0.6 \cdot V_S$. This analysis
 631 was performed by Kaneko and Shearer (2015) for a range of rupture scenarios: circular
 632 or elliptical and symmetric or asymmetric. They found that decreasing the rupture speed
 633 can produce deviations of up to 2.5 times higher in terms of stress drop depending on the
 634 model and the wave phase (P or S). Average RSF estimates of rupture velocities were much
 635 lower $0.6 \cdot V_S$. From Table 1 in Kaneko and Shearer (2015), we updated the estimates from
 636 Selvadurai (2019), which minimized the difference between the kinematic (triangles) and
 637 RSF (circles) estimates of source properties. Original kinematic estimates are scaled by
 638 those from an asymmetric circular asperity model with rupture velocity $0.6 \cdot V_S$ leading to
 639 an increase in seismic moment by 2.63 for P wave estimates and 2.74 for S waves estimates.

640 Figure 12(c) displays the constitutive shear stress versus slip behaviour for a large
 641 random asperity. For reference, we mark the levels of $D_{c,low}$, $D_{c,eq}$ and $D_{c,high}$. The term
 642 $D_{c,eq}$, or equivalent critical slip weakening distance, appears to be a representative critical
 643 slip weakening distance that always lies between the two D_c limits but will likely vary for
 644 each rupture as a function of the ratio of high to low resistance of the interface participating
 645 in rupture. Looking at the relationship between G' and slip, we see that it appears to have
 646 a “kink”. This kink is observed at about the slip level of $D_{c,eq}$.

647 4 Discussion

648 We have summarized findings from a well-documented laboratory experiment (Selvadurai
 649 & Glaser, 2015a, 2017; Selvadurai, 2019) that displayed complex nucleation behavior:
 650 preparatory slow preslip accompanied by intermittent localized seismicity from the same
 651 sections of the frictional interface (see Figure 1). A RSF model was developed to examine
 652 the complex frictional behavior using the rate- and state-dependent constitutive framework.
 653 The model accounted for wear observed from *a posteriori* measurements of roughness on the
 654 slider block surface that was well characterized in terms of a bimodal Gaussian distribution
 655 of surface roughness (Figure 2(a)). Attributes of our worn interface show a distinct polished
 656 surface embedded in a rougher surface, a feature that may be similar to the polished fault
 657 mirrors (FMs) observed on natural outcrops (see Figures 2(e) and (f)).

658 A cutting plane method (Figure 3) was used to mathematically quantify the spatial
 659 variation between smooth and rough sections. Two sets of RSF properties were chosen
 660 based on the fact that smooth surfaces have lower critical slip weakening distance D_c than
 661 rougher sections and the level of heterogeneity was investigated. The models showed com-
 662 plex behaviour (Figure 7) that differed from the homogeneous case (Figure 5); this could
 663 explain the experimental observation of concomitant slow slip and localized seismicity. We
 664 developed algorithms to isolate ruptures (Figures 8 and 9). These allowed us to estimate a
 665 range of source properties, such as scalar seismic moment (M_0), rupture length scale (L_r),
 666 seismic slip (δ), stress drop ($\Delta\tau$), fracture energy (G') and frequency-magnitude distribu-
 667 tions (FMD) of five different D_c -models and a composite-model (Figures 10, 11 and 12).
 668 These calculations were compared to independently estimated seismological source proper-
 669 ties made from interpretation of the seismic waves (Selvadurai, 2019).

670 4.1 ‘Cascade-up’ nucleation behavior

671 Our model exhibits a wide range of behaviors, ranging from periodic (O1) to increas-
 672 ingly disordered (O10 to O18.5) then returning to more ordered (O20) (see Figure 7). In
 673 Figure 5 we observe that homogeneous rupture is well-behaved, exhibiting periodic stick-slip
 674 events at constant recurrence time. In the model, we assume periodic boundary conditions.
 675 This implies that if a rupture is not arrested within the mesoscopic region and reaches the
 676 boundary it would theoretically continue grow and rupture the full macroscopic region –
 677 cascading-up and creating a system-wide stick-slip event that was observed experimentally
 678 (Figure 1(b)).

679 We link full-rupture events to cascade-up nucleation processes forming from the ini-
 680 tiation of a stuck patch (Noda et al., 2013; Selvadurai & Glaser, 2017; McLaskey, 2019).
 681 This assumption is plausible when looking at the hypocenter of the full-fault rupture (i.e.
 682 system-wide stick-slip event) measured experimentally in Selvadurai and Glaser (2015a).
 683 These were consistently located in the region near the roughness measurement (magenta
 684 star in Fig. 7 and 8 in Selvadurai & Glaser, 2015a). Moreover, this model appears to
 685 have produced rate-dependent cascade-up nucleation where foreshocks are a byproduct of
 686 the slow nucleation process but also small seismic ‘ignitions’ can initiate the full-rupture as
 687 described by rate-dependent cascade-up model (Noda et al., 2013; McLaskey, 2019).

688 In Figure 11, the two types of end-member behaviors are highlighted: ‘creep dominated’
689 and ‘stick-slip dominated’. Stick-slip dominated behavior is described as supporting local-
690 ized foreshocks sequences but also small events would cascade-up and trigger full ruptures.
691 The creep dominated events from the O20 model were localized but they never developed
692 into full ruptures. The D_c -models O10 and O15 exhibited foreshock sequences that were
693 followed by a cascade-up into full ruptures (Figure 5), whereas O20 showed constrained
694 ruptures that did not cascade-up.

695 Both the O10 and O20 models had identical level of normal stress σ_n leading to similar
696 levels of peak and residual shear stress levels but the variations in D_c imposed differences in
697 the weakening rates and fracture energy on the rough sections of each model. Therefore the
698 order of the model was directly related to the the level of heterogeneity in fracture energy for
699 our models. We found that for relatively low levels of fracture energy heterogeneity faults
700 displayed a stick-slip-dominant behavior (foreshocks that can potentially cascade-up) and,
701 once the heterogeneity is large enough, a creep-dominant behavior is observed. Hierarchical
702 heterogeneity in fracture energy has been proposed by others (Ide & Aochi, 2005; Aochi &
703 Ide, 2014, 2017) and will be discussed later.

704 While we cannot confirm an exact wear mechanism that may produce flat sections
705 or increase the level of heterogeneity between smooth and rough sections, one hypothesis
706 is that certain sections of the fault are more prone to flattening (ironing) and others will
707 develop particles of gouge. Flattening, or ‘ironing’, of asperities due to adhesive wear has re-
708 cently been investigated using a material independent framework (Aghababaei et al., 2016).
709 Physics-based numerical simulations found a critical length scale describing the deforma-
710 tion mechanisms of interacting asperities. At length scales below a critical value, asperities
711 flatten inelastically, dependent on the size of the asperity junction, the work of adhesion of
712 the bulk material, and the maximum elastic strain energy that can be stored at a contact.
713 This explanation fits observations made by Siman-Tov et al. (2013) and others that studied
714 fault mirror formation in the laboratory. Brown and Scholz (1986) found that flattened
715 patches could form upon the closure the interface indicating significant plastic flow at the
716 highest points on the surface, albeit at smaller length scales than mirror surfaces studied
717 and produced in the laboratory (Fondriest et al., 2013; Siman-Tov et al., 2013; Tisato et
718 al., 2012; Siman-Tov et al., 2015).

719 Candela and Brodsky (2016) proposed plastic yielding, or grooving length scale that is
720 controlled by the specific aspect ratio of roughness asperities on the fault. They hypothesised
721 that the minimum grooving length scale is related to the critical slip weakening parameter
722 D_c arguing that plastic yielding combined with scale-dependent roughness define the process
723 that sets the scale of the relevant asperities. This argument is similar to our arguments and
724 links variations in worn distribution of D_c presented here to seismicity on larger length scales
725 in natural faults. While temperature, fluid and chemical processes observable on natural
726 faults make the conjecture that simple laboratory experiments of solid friction have no
727 bearing on real faults. Candela and Brodsky (2016) suggests the opposite and the preserved
728 fingerprint on natural fault surfaces of the fundamental process governing solid friction.

729 4.2 Dominant asperity

730 All models hinged about the behavior of specific section of the fault from $x = 5$ mm
731 to 8 mm, we referred to as the dominant asperity (Figure 8(b) and (c)). In all models,
732 this section produced localized events. With lower levels of heterogeneity (O10 and O15),
733 foreshocks were produced from this asperity that also possessed the potential of cascading
734 runaway rupture. In Supplemental Sections S3, we show spatio-temporal evolution of slip of
735 O10 and the O15 full-ruptures, in which breakdown occurs in a similar manner – nucleating
736 each time from the dominant asperity. This dominant asperity behaved at times as an
737 ignition site for the nucleation of gross fault rupture and this may be similar to behaviors
738 of asperities predisposed to seismicity in nature.

739 This type of behavior may explain the observations in the Naka-Oki region in eastern
740 Japan (Okuda & Ide, 2018a) and the Tohoku–Hokkaido subduction zone, Japan (Ide, 2019).
741 Where earthquakes shared almost identical growth offering patterns for repeating events of
742 various sizes. This observation appears to be consistent with our model, an explanation that
743 repeater asperities that routinely produce $M_w \sim 2$ could have structures in that sometimes
744 allow for it to cascade-up to $M_w \sim 4.8$ (Okuda & Ide, 2018b). These authors hypothesize
745 that a hierarchical structure exists (as depicted in fig. 5 of Okuda & Ide, 2018a), possibly
746 due to heterogeneity in the fracture energy (Ide & Aochi, 2005; Aochi & Ide, 2014, 2017).
747 Our model agrees with this hypothesis and heterogeneity in fracture energy is provided in
748 the form of polished smooth sections in a rougher interface that does not exhibit large out
749 of plane roughness-induced barriers.

750 We also observe interesting behavior surrounding the unlocking sequence of the dom-
 751 inant asperity in Figure 8(c). For clarity, the temporal unlocking sequence for the O17.5
 752 model were enumerated in ascending order from 1 to 4. Below the spatio-temporal slip
 753 evolution (red and blue isochrons), we show the spatial length of each rupture. We can see
 754 that each rupture overlaps the previous rupture, a phenomenon was also observed by Okuda
 755 and Ide (2018b) and referred to as ‘streaking’, which they claimed explained the patches
 756 of differing sizes possessing some hierarchical structure. This also might be similar to the
 757 dynamic precursor detachment fronts observed experimentally on fault analogs (Rubinstein
 758 et al., 2004, 2006) and the breakdown fronts seen on granite-granite interfaces by (Ke et al.,
 759 2018). Okuda and Ide (2018b) attribute this specific rupture process to subtle differences
 760 in the physical conditions of the fault interface, which appear to be consistent with a fault
 761 interface consisting of a series of hierarchical structures. Our model produced foreshocks in
 762 a broad sense (Mogi, 1985) and was due to the patchy distribution of fracture energy on our
 763 smooth/rough frictional fault idealization.

764 Mogi (1963) inferred the crustal structure in Japan from the records of seismic gaps,
 765 swarms, aftershocks and foreshocks (see also Mogi, 1985). He found that regions with
 766 less fracturing appear to correlate to the newer observations of repeating strikers and the
 767 cascade-up style seismic signatures discussed here (Okuda & Ide, 2018a, 2018b; Ide, 2019).
 768 As noted by Wang and Bilek (2014), there are positive correlation between large events
 769 and smooth subducting segments of seafloor that may become increasingly smoothed (over
 770 millions of years) by wearing of the interface with the large amount of sediments. While
 771 more study is required, producing frictional models with proper stochastic distribution of
 772 frictional properties that are able to reproduce the complex observational behavior (streaking
 773 repeaters capable of cascade-up style-behavior) should be a point of discussion in the future
 774 (see further discussion in Section 4.7).

775 **4.3 Repeating-like behavior**

776 In contrast to the cascade-up behavior discussed above, the dominant asperity ($x =$
 777 5 mm to 8 mm) also showed quite regular behavior when the level of heterogeneity was
 778 increased to O20. Spatio-temporal evolution of slip from 300 s to 600 s for the O20 model
 779 is also given in Supplemental Section S3. For this model, the average shear stress and
 780 slip rates remained near steady state (equation eq7) and the only deviation came from the
 781 local increase in slip rate during ruptures of the dominant asperity. In Figure 11 we refer

782 to this as ‘creep-dominated’. For our creep-dominated fault, any event produced by the
 783 dominant asperity was easily arrested by the rougher surroundings, which in the model,
 784 were actually regions exhibiting relatively larger fracture energy. This ‘creep-dominated’
 785 behavior is similar to that observed for repeating earthquakes in nature (e.g., Beeler et al.,
 786 2001; Uchida, 2019)

787 Models used to understand repeating earthquakes typically involve a circular asperity
 788 embedded on a planar fault, where the asperity is relatively locked with respect to the
 789 creeping region that loads a resistive asperity. When studied using RSF laws, the creeping
 790 region is typically given velocity-strengthening (VS, $(a-b)>0$) properties and the asperity is
 791 velocity-weakening (VW, $(a-b)<0$) (N. Kato, 2003; Chen & Lapusta, 2009). In our models,
 792 seismicity only occurs on the VW asperity and their ability to trigger more complex behavior,
 793 e.g. a cascade-up style rupture, cannot exist unless additional heterogeneity to VW regions
 794 are specified. Noda et al. (2013) looked at the behavior of smaller VW asperities embedded
 795 on a larger VW asperity while varying ratios of RSF properties and found complex model
 796 behavior. Our model finds that, due to the heterogeneity the in polished-to-rough surface, we
 797 can actually host constrained repeating earthquakes in an entirely VW region that depends
 798 on the level of heterogeneity. As heterogeneity increases between the polished and rough
 799 sections, repeating events and creep-dominated behavior may become more apparent.

800 4.4 Nucleation/arrest of crack-like ruptures

801 Figures 8(d) and (e) summarized the behavior of a crack-like rupture typically seen
 802 on the dominant asperity. Nucleation of the precursory events mostly occurred on the
 803 boundaries between the smooth-rough transition on the VW interface. This type of behavior
 804 has been observed in a larger scale 2D RSF simulation of the Parkfield section of the San
 805 Andreas Fault, CA, USA (Barbot et al., 2012), in conceptual models of interacting asperities
 806 (N. Kato, 2003) and complex megathrust subduction zones (Kaneko et al., 2010); however,
 807 nucleation in these models occur frequently at a VS-VW transition.

808 From Figure 9, we see that the smoother ruptures were more efficient, reaching higher
 809 slip rates, having higher stress drop and producing less fracture energy. Slower rupture
 810 speeds coupled with less stress drop and higher fracture energies occurred on sections that
 811 had a “rough” parameterization, which was as expected. The complex interaction of how
 812 the rupture that propagated on both a polished and rough interface was apparent even as

813 it decelerated, when the P waves stopping phase was observed (Madariaga, 1976). This
 814 stopping phase appears to be reflected or emanating from the smooth-rough boundaries.

815 **4.5 Dynamic RSF source properties**

816 The model displays great complexity at the mesoscopic (Figure 7) and microscopic
 817 scales (Figures 8 and 9). Dynamic RSF source estimates of moment to source length scale
 818 followed the standard $M_0 \propto L_r^3$, which also matched kinematic estimates in Selvadurai
 819 (2019). While the dynamic and kinematic source estimates highlighted here differ slightly,
 820 the magnitude and trends between estimates are similar even though the problem is ap-
 821 proached from two different modeling frameworks. Comparing these two different models is
 822 an important step towards validating the effectiveness of each model and understanding how
 823 to link precursory seismicity to the nucleation phase on fault analogs. Identical validation
 824 efforts have been used for RSF models looking at repeating earthquakes in Parkfield, CA
 825 (Chen & Lapusta, 2009).

826 Stress drop is dependent on the rupture velocity (V_r) (Kaneko & Shearer, 2015). We
 827 found our crack-like rupture to be much slower ($0.6 \cdot V_S$) than those typically used in kine-
 828 matic approaches, where kinematic shear crack models assume rupture velocities between 0.9
 829 and $1.0 \cdot V_S$ (Cocco et al., 2016; Selvadurai, 2019). With this additional knowledge, updates
 830 to our original kinematic estimates were made by applying correction factors from numer-
 831 ical studies performed by Kaneko and Shearer (2015). This correction factor increased the
 832 correlation between kinematic estimates and RSF estimates. Using more accurate estimates
 833 of rupture velocity when estimating source features via kinematic crack-models should be
 834 done carefully and investigated in more detail (e.g. McGuire & Kaneko, 2018).

835 Fracture energy G' versus slip was compared for two types of model (D_c and composite)
 836 with scaling relationships in the lab (S_L) and field (AR). The D_c model followed the AR
 837 scaling relationship more closely, which we attribute to the fact that ruptures occurred with
 838 the rougher (more resistive) portions more than in the composite model. Perhaps this was
 839 due to the description of heterogeneity in the models. The D_c -model had a constant shear
 840 strength and, therefore, heterogeneity in both the slip-weakening rate and fracture energy on
 841 the polished/rough sections controlled the source properties. The Composite-model added
 842 to the complexity by including normal stress variability, causing an additional heterogeneity
 843 in the shear strength of the fault (see equation eq5). This additional complexity caused

844 more localized seismicity that occurred because of larger contrasts in slip-weakening rate
 845 and less contrast in the fracture energy between the polished and rough sections. This is
 846 clearly seen in the O20 and O20-C spatio-temporal distributions of slip that shown in detail
 847 in Supplemental Figures S3.4 and S3.5, respectively. The composite model nucleated more
 848 events but, similar to the less complex model, there was no cascade-up rupture. In the
 849 composite model, geometrically smaller smooth sections could nucleate rupture but they
 850 would arrest due to the lower strength of the rough region. The purpose of this study was
 851 to provide a reasonable parameter space (Figure 4) based on a suite of experiments that,
 852 when combined with a novel RSF model, provides insight into the potential behaviors of
 853 worn faults in nature.

854 **4.6 Effect of fracture energy heterogeneity on FMDs**

855 Analysis of the FMDs showed that creeping faults (O20 and O20-c) had higher b_{GR} -
 856 and a_{GR} -values than stick-slip dominant faults (O-10 and O15). A gradual transition was
 857 observed from both low to high a_{GR} - and b_{GR} -values as the heterogeneity in fracture energy
 858 was increased. This observation follows studies in natural tectonic settings where creeping
 859 sections were found to have higher b-values than locked section prone to larger earthquake
 860 (Amelung & King, 1997; Tormann et al., 2014). Goebel et al. (2013) found that tempo-
 861 ral decreases in laboratory estimates of b-values occurred moments leading up to larger
 862 stick-slip events, a phenomena that has been observed in natural tectonic settings prior to
 863 large megathrust events (Tormann et al., 2015; Gulia et al., 2016; Gulia & Wiemer, 2019).
 864 Our model suggests that lower b-values may occur on faults that also experience foreshock
 865 behavior and both observations can be reconciled by a hierarchical structure of the fault
 866 that exhibits low (but distinct) variations in fracture energy distribution, which is a point
 867 of study moving forward.

868 Completeness in our model is associated with the minimum size of resolvable earthquake
 869 defined by the mesh scheme and solution convergence (Supplemental Section S1). This
 870 differs from the field where M_c is affected by the fact that the recording network is only
 871 capable of recording a fraction of all events for magnitudes smaller (Wiemer & Wyss, 2002).
 872 By definition, the Gutenberg-Richter law is scale-invariant above the magnitude of the
 873 completeness threshold (M_c). Below this threshold, the size and occurrence of seismicity
 874 is scale-variant. From a statistical perspective, events falling below M_c are not used and
 875 using more involved methods that investigate the catalog behavior near and below M_c will

876 be useful (Mignan, 2012, 2020). While scale invariance is produced by our model, a large
877 number of events fall below this threshold and are likely due to the scale-variant mechanism
878 associated with the smoothing of high asperities during the wearing process. More extensive
879 studies will be needed but we note scale variant features, such as the dominant asperity,
880 had important impact on critical aspects of nucleation physics, such as the generation of
881 foreshocks and cascade-up style failure, which may be useful for earthquake forecasting and
882 prediction.

883 Understanding whether regions susceptible to foreshocks and rate-dependent cascade-up
884 style failure would impose a break in the empirically observed scaling of seismicity (Scholz,
885 1997) or if they simply correspond to the statistical superposition of power law brittle-failure
886 type process and a point repeater-like process at a characteristic length scale, could help
887 us understand how these potentially important hierarchical structures affect our ability to
888 interpret statistical tools for hazard and risk in these regions.

889 **4.7 RSF properties on worn sections of faults**

890 In Section 1.3, we highlighted findings from tribology in which wearing of surfaces
891 can produce nanometrically smooth regions in an overriding rougher surface that is well-
892 characterized by the bi-modal Gaussian PDF of surface height. These polished sections have
893 also been linked to fault mirrors through laboratory tests under a range of conditions (slow
894 and fast sliding and at high-temperature). Laboratory experiments give explanations as to
895 why these FMs exist on exposed outcrops but do not give the extent of how large they may
896 grow due to constraints of typical laboratory studies that produce them. Unfortunately, our
897 understanding of polished fault mirrors from exposed outcrops is constrained by our ability
898 to observe them; an obvious limitation exists when we compared the volume of exposed
899 outcrops to the volume of active faults producing seismicity in nature.

900 Our model suggests that the scale of polished sections to rough sections is impor-
901 tant; correspondingly, we conjecture that attempting to capture this using the single fractal
902 measurement of the Hurst exponent is not adequate (the scale at which needs more investi-
903 gation). Since the mirrors in our model required a bi-modal Gaussian distribution of surface
904 heights, new research into fractal characterization of such surfaces by Hu et al. (2019a) sug-
905 gests that a bi-fractal distribution in roughness is more representative (Leefe et al., 1998;
906 Pawlus, 2008). These surfaces have already been shown to influence characteristics of acous-

907 tic emission energy release upon sliding (Fan et al., 2010; Hu et al., 2019b) but these results
908 are recent and more investigation is required. Bi-modal Gaussian and b-fractal stochastic
909 descriptions of frictional parameters may help us understand complex frictional behavior,
910 such as faults where rate-dependent cascade-up physics have been observed.

911 5 Conclusions

912 We developed RSF to capture slow aseismic transients coupled with localized foreshocks
913 and compared this to similar behavior observed in a concerted laboratory experiment on a
914 fault analog. Heterogeneity was necessary and prescribed using the worn surface roughness
915 that displayed a bimodal Gaussian distribution of surface heights. We discretized smooth
916 and rough faults using an understanding the micro-mechanics of the critical slip D_c where
917 smooth sections have lower values. This resulted in polished sections (mirrors) producing
918 small ruptures, whereas rougher sections hosted aseismic slip.

919 The behavior of the fault varied between creep-like to stick-slip dominated and depended
920 on the level of heterogeneity in the fracture energy. Small localized events were particularly
921 interesting around a dominant asperity that produced seismicity in every simulation and
922 appeared to control cascade-up-breakdown of the fault when the level of fracture energy
923 heterogeneity was low.

924 Seismic source properties were validated against independent kinematic estimates from
925 elastodynamic ground motions. Rupture velocity obtained from the RSF models estimated
926 that subsonic ruptures propagated at speeds close to $V_r = 0.6 \cdot V_S$. This was used to
927 adjust kinematic source properties by Selvadurai (2019) for the slower crack-like ruptures.
928 Validating the RSF source properties was deemed sufficient for a first-order understanding of
929 the modeled frictional heterogeneity that may explain simultaneous foreshocks and aseismic
930 preslip. We believe that this should be further explored in more robust parametric studies.

931 Worn faults observed in nature have the form of fault mirrors but it is unclear how
932 they truly evolve over geologic time, their spatial extent and how this evolution affects the
933 frictional response of a shear principal slip zone. In our wear-based model, changes in the
934 level of heterogeneity in fracture energy caused end-member behavior from creep to stick-
935 slip dominant. Future experiments will need to investigate this behavioral evolution and
936 potentially update the stochastic descriptions of frictional parameters on faults that contain
937 FMs.

Acknowledgments

We would like to thank T. Yamaguchi, L. Villiger, B. Edwards T. Tormann, P. Bhattacharya and A. Mignan who provided important discussion points regarding the analysis. Key insights into simulations presented here are given by J.-P. Ampuero. This research was supported by: JSPS KAKENHI Grant Number JP16H06478 in Scientific Research on Innovative Areas “Science of Slow Earthquakes”. Computational resources were provided by the Information Technology Division and Extreme Computing Research Center (ECRC) at KAUST. Funding for parts of this research was provided by the National Science Foundation Grant CMMI-1131582 awarded to SDG at the University of California, Berkeley. Funding for PAS was provided through the OFES Project: EDGAR - Dimensionnement du réseau de fractures dans les réservoirs géothermaux (Contract SI/501495-01). PMM’s contribution to this study and a research visit of PAS to KAUST was supported by KAUST research grant BAS/1/1339-01-01. Finally, the authors assume full responsibility for the comments and concepts presented in the paper.

All data sets required to reproduce the results presented here are freely available at this site (doi.org/10.3929/ethz-b-000405620). Please contact the corresponding author for access.

References

- Abercrombie, R. E., & Rice, J. R. (2005). Can observations of earthquake scaling constrain slip weakening? *Geophysical Journal International*, *162*(2), 406–424. Retrieved from <http://dx.doi.org/10.1111/j.1365-246X.2005.02579.x> doi: 10.1111/j.1365-246X.2005.02579.x
- Adachi, K., & Kato, K. (2000). Formation of smooth wear surfaces on alumina ceramics by embedding and tribo-sintering of fine wear particles. *Wear*, *245*(1), 84–91. Retrieved from <http://www.sciencedirect.com/science/article/pii/S0043164800004683> doi: [http://dx.doi.org/10.1016/S0043-1648\(00\)00468-3](http://dx.doi.org/10.1016/S0043-1648(00)00468-3)
- Aghababaei, R., Warner, D. H., & Molinari, J. F. (2016). Critical length scale controls adhesive wear mechanisms. *Nature Communications*, *7*(11816).
- Aki, K. (1966). Generation and propagation of G waves from the Niigata Earthquake of June 16, 1964. Part 2. Estimation of earthquake movement, released energy, and stress-strain drop from the G wave spectrum. *Bull. Earthq. Res. Inst.*, *44*, 73–88. Retrieved from <https://ci.nii.ac.jp/naid/10006221613/en/>

- 970 Amelung, F., & King, G. (1997, September). Earthquake scaling laws for creeping and
 971 non-creeping faults. *Geophysical Research Letters*, *24*(5), 507–510. Retrieved from
 972 <https://doi.org/10.1029/97GL00287> doi: 10.1029/97gl00287
- 973 Ampuero, J. P., & Rubin, A. M. (2008). Earthquake nucleation on rate and state faults:
 974 Aging and slip laws. *Journal of Geophysical Research*, *113*, B01302. doi: 10.1029/
 975 2007JB005082
- 976 Aochi, H., & Ide, S. (2014). Ground motions characterized by a multi-scale heterogeneous
 977 earthquake model. *Earth, Planets and Space*, *66*(42).
- 978 Aochi, H., & Ide, S. (2017, July). Role of multiscale heterogeneity in fault slip from quasi-
 979 static numerical simulations. *Earth, Planets and Space*, *69*(1), 94. Retrieved from
 980 <https://doi.org/10.1186/s40623-017-0676-5>
- 981 Barbot, S., Lapusta, N., & Avouac, J. (2012). Under the Hood of the Earthquake Machine:
 982 Toward Predictive Modeling of the Seismic Cycle. *Science*, *336*(6082), 707-710. Re-
 983 trieved from <http://www.sciencemag.org/content/336/6082/707.abstract> doi:
 984 10.1126/science.1218796
- 985 Beeler, N. M., Lockner, D. L., & Hickman, S. H. (2001, 12). A Simple Stick-Slip and
 986 Creep-Slip Model for Repeating Earthquakes and its Implication for Microearthquakes
 987 at Parkfield. *Bulletin of the Seismological Society of America*, *91*(6), 1797–1804.
 988 Retrieved from <https://doi.org/10.1785/0120000096> doi: 10.1785/0120000096
- 989 Ben-David, O., Cohen, G., & Fineberg, J. (2010). The Dynamics of the Onset of Frictional
 990 Slip. *Science*, *330*(6001), 211–214. doi: 10.1126/science.1194777
- 991 Ben-Zion, Y. (2008, August). Collective behavior of earthquakes and faults:
 992 Continuum-discrete transitions, progressive evolutionary changes, and different dy-
 993 namic regimes. *Reviews in Geophysics*, *46*(4). Retrieved from [https://doi.org/](https://doi.org/10.1029/2008RG000260)
 994 [10.1029/2008RG000260](https://doi.org/10.1029/2008RG000260) doi: 10.1029/2008rg000260
- 995 Beroza, G. C., & Ellsworth, W. L. (1996). Properties of the seismic nucleation phase.
 996 *Tectonophysics*, *261*(1-3), 209–227. doi: [http://dx.doi.org/10.1016/0040-1951\(96\)](http://dx.doi.org/10.1016/0040-1951(96)00067-4)
 997 00067-4
- 998 Berthoude, P., Baumberger, T., G'Sell, C., & Hiver, J. M. (1999). Physical analy-
 999 sis of the state- and rate-dependent friction law: Static friction. *Physical Review*
 1000 *B: Condensed Matter and Materials Physics*, *59*(22), 14313–14327. doi: 10.1103/
 1001 PhysRevB.59.14313
- 1002 Bhattacharya, P., Rubin, A. M., Bayart, E., Savage, H. M., & Marone, C. (2015). Critical

- 1003 evaluation of state evolution laws in rate and state friction: Fitting large velocity
 1004 steps in simulated fault gouge with time-, slip-, and stress-dependent constitutive
 1005 laws. *Journal of Geophysical Research: Solid Earth*, *120*(9), 6365–6385. doi: 10.1002/
 1006 2015JB012437
- 1007 Borucki, L. (2002). Mathematical modeling of polish-rate decay in chemical-mechanical
 1008 polishing. *Journal of Engineering Mathematics*, *43*(2), 105–114. Retrieved from
 1009 <http://dx.doi.org/10.1023/A:1020305108358> doi: 10.1023/A:1020305108358
- 1010 Borucki, L. J., Witelski, T., Please, C., Kramer, P. R., & Schwendeman, D. (2004).
 1011 A theory of pad conditioning for chemical-mechanical polishing. *Journal of Engi-
 1012 neering Mathematics*, *50*(1), 1–24. Retrieved from [http://dx.doi.org/10.1023/B:
 1013 ENGI.0000042116.09084.00](http://dx.doi.org/10.1023/B:ENGI.0000042116.09084.00) doi: 10.1023/B:ENGI.0000042116.09084.00
- 1014 Bouchon, M., Durand, V., Marsan, D., Karabulut, H., & Schmittbuhl, J. (2013, April). The
 1015 long precursory phase of most large interplate earthquakes. *Nature Geoscience*, *6*(4),
 1016 299–302. Retrieved from <http://dx.doi.org/10.1038/ngeo1770>
- 1017 Bouchon, M., Karabulut, H., Aktar, M., Ozalaybey, S., Schmittbuhl, J., & Bouin, M. P.
 1018 (2011). Extended nucleation of the 1999 M_w 7.6 Izmit earthquake. *Science*, *331*(6019),
 1019 877–880. doi: 10.1126/science.1197341
- 1020 Bouissou, S., Petit, J. P., & Barquins, M. (1998, February). Normal load, slip rate
 1021 and roughness influence on the polymethylmethacrylate dynamics of sliding 1. Sta-
 1022 ble sliding to stick-slip transition. *Wear*, *214*(2), 156–164. Retrieved from [http://
 1023 www.sciencedirect.com/science/article/pii/S0043164897002421](http://www.sciencedirect.com/science/article/pii/S0043164897002421)
- 1024 Brodsky, E. E., Gilchrist, J. J., Sagy, A., & Collettini, C. (2011). Faults smooth gradually as
 1025 a function of slip. *Earth and Planetary Science Letters*, *302*, 185–193. Retrieved from
 1026 <http://www.sciencedirect.com/science/article/pii/S0012821X10007624> doi:
 1027 doi.org/10.1016/j.epsl.2010.12.010
- 1028 Brodsky, E. E., Kirkpatrick, J. D., & Candela, T. (2016). Constraints from fault roughness
 1029 on the scale-dependent strength of rocks. *Geology*, *44*(1), 19–22.
- 1030 Brodsky, E. E., & Lay, T. (2014). Recognizing Foreshocks from the 1 April 2014 Chile
 1031 Earthquake. *Science*, *344*(6185), 700–702. doi: 10.1126/science.1255202
- 1032 Brown, S. R., & Scholz, C. H. (1986, September). closure of rock joints. *Journal of
 1033 Geophysical Research Solid Earth*, *91*(B5), 4939–4948. Retrieved from [https://doi
 1034 .org/10.1029/JB091iB05p04939](https://doi.org/10.1029/JB091iB05p04939) doi: 10.1029/jb091ib05p04939
- 1035 Buijze, L., Guo, Y., Niemeijer, A. R., Ma, S., & Spiers, C. J. (2020). Nucleation of stick-slip

- 1036 instability within a large-scale experimental fault: Effects of stress heterogeneities due
 1037 to loading and gouge-layer compaction. *Journal of Geophysical Research: Solid Earth*,
 1038 *n/a(n/a)*, e2019JB018429. Retrieved from [https://agupubs.onlinelibrary.wiley](https://agupubs.onlinelibrary.wiley.com/doi/abs/10.1029/2019JB018429)
 1039 [.com/doi/abs/10.1029/2019JB018429](https://agupubs.onlinelibrary.wiley.com/doi/abs/10.1029/2019JB018429) doi: 10.1029/2019JB018429
- 1040 Bürgmann, R. (2004). Warning signs of the Iquique earthquake. *Nature*, *512*, 258–259.
- 1041 Bürgmann, R., Schmidt, D., Nadeau, R. M., d’Alessio, M., Fielding, E., Manaker, E., ...
 1042 Murray, M. H. (2000). Earthquake Potential Along the Northern Hayward Fault,
 1043 California. *Science*, *289*, 1178–1182.
- 1044 Candela, T., & Brodsky, E. E. (2016). The minimum scale of grooving on faults. *Geology*,
 1045 *44*(8), 603–606.
- 1046 Candela, T., Renard, F., Bouchon, M., Marsan, D., Schmittbuhl, J., & Voisin, C.
 1047 (2009). Characterization of Fault Roughness at Various Scales: Implications of Three-
 1048 Dimensional High Resolution Topography Measurements. *Pure and Applied Geo-*
 1049 *physics*, *166*, 1817–1851. doi: 10.1007/s00024-009-0521-2
- 1050 Chen, T., & Lapusta, N. (2009). Scaling of small repeating earthquakes explained by interac-
 1051 tion of seismic and aseismic slip in a rate and state fault model. *Journal of Geophysical*
 1052 *Research: Solid Earth*, *114*(B1). Retrieved from [https://agupubs.onlinelibrary](https://agupubs.onlinelibrary.wiley.com/doi/abs/10.1029/2008JB005749)
 1053 [.wiley.com/doi/abs/10.1029/2008JB005749](https://agupubs.onlinelibrary.wiley.com/doi/abs/10.1029/2008JB005749) doi: 10.1029/2008JB005749
- 1054 Ciavarella, M. (2016). On the effect of wear on asperity height distributions, and
 1055 the corresponding effect in the mechanical response. *Tribology International*, *101*,
 1056 164–167. Retrieved from [http://www.sciencedirect.com/science/article/pii/](http://www.sciencedirect.com/science/article/pii/S0301679X16300858)
 1057 [S0301679X16300858](http://www.sciencedirect.com/science/article/pii/S0301679X16300858) doi: <http://doi.org/10.1016/j.triboint.2016.04.031>
- 1058 Cocco, M., Tinti, E., & Cirella, A. (2016). On the scale dependence of earthquake stress
 1059 drop. *Journal of Seismology*, *20*, 1151–1170. doi: [https://doi.org/10.1007/s10950-016](https://doi.org/10.1007/s10950-016-9594-4)
 1060 [-9594-4](https://doi.org/10.1007/s10950-016-9594-4)
- 1061 Dieterich, J. H. (1978). Preseismic fault slip and earthquake prediction. *Journal of Geo-*
 1062 *physical Research*, *83*(B8), 3940–3948. doi: 10.1029/JB083iB08p03940
- 1063 Dieterich, J. H. (1979). Modeling of rock friction: 1. Experimental results and con-
 1064 stitutive equations. *Journal of Geophysical Research*, *84*(B5), 2161–2168. doi:
 1065 10.1029/JB084iB05p02161
- 1066 Dieterich, J. H. (1992). Earthquake nucleation on faults with rate-and state-
 1067 dependent strength. *Tectonophysics*, *211*(1), 115–134. Retrieved from [http://](http://www.sciencedirect.com/science/article/pii/004019519290055B)
 1068 www.sciencedirect.com/science/article/pii/004019519290055B doi: [https://](https://doi.org/10.1016/0040-1951(92)90055-B)

- doi.org/10.1016/0040-1951(92)90055-B
- 1069
1070 Dodge, D. A., Beroza, G. C., & Ellsworth, W. L. (1995). Foreshock sequence of the
1071 1992 Landers, California, earthquake and its implications for earthquake nucleation.
1072 *Journal of Geophysical Research*, *100*(B6), 9865–9880. doi: 10.1029/95JB00871
- 1073 Dodge, D. A., Beroza, G. C., & Ellsworth, W. L. (1996). Detailed observations of California
1074 foreshock sequences: Implications for the earthquake initiation process. *Journal of*
1075 *Geophysical Research*, *101*(B10), 22371–22392. doi: 10.1029/96JB02269
- 1076 Dreger, D., Nadeau, R. M., & Chung, A. (2007). Repeating earthquake finite source models:
1077 Strong asperities revealed on the San Andreas fault. *Journal of Geophysical Research*,
1078 *34*, L23302. doi: 10.1029/2007GL031353
- 1079 Dunham, E. M., Belanger, D., Cong, L., & Kozdon, J. E. (2011). Earthquake Ruptures
1080 with Strongly Rate-Weakening Friction and Off-Fault Plasticity, Part 2: Nonplanar
1081 Faults. *Bulletin of the Seismological Society of America*, *101*(5), 2308. Retrieved from
1082 <http://dx.doi.org/10.1785/0120100076> doi: 10.1785/0120100076
- 1083 Ellsworth, W. L., & Beroza, G. C. (1995). Seismic evidence for an earthquake nucleation
1084 phase. *Science*, *268*(5212), 851–855. doi: 10.1126/science.268.5212.851
- 1085 Fan, Y., Gu, F., & Ball, A. (2010, February). Modelling acoustic emissions generated by
1086 sliding friction. *Wear*, *268*(5), 811–815. Retrieved from [http://www.sciencedirect](http://www.sciencedirect.com/science/article/pii/S0043164809006322)
1087 [.com/science/article/pii/S0043164809006322](http://www.sciencedirect.com/science/article/pii/S0043164809006322)
- 1088 Fang, Z., & Dunham, E. M. (2013). Additional shear resistance from fault roughness and
1089 stress levels on geometrically complex faults. *Journal of Geophysical Research: Solid*
1090 *Earth*, *118*(7), 3642–3654. doi: 10.1002/jgrb.50262
- 1091 Fineberg, J., & Bouchbinder, E. (2015, November). Recent developments in dynamic frac-
1092 ture: some perspectives. *International Journal of Fracture*, *196*(1), 33–57. Retrieved
1093 from <https://doi.org/10.1007/s10704-015-0038-x>
- 1094 Fondriest, M., Smith, S., Candela, T., Nielsen, S. B., Mair, K., & Di Toro, G. (2013, 11).
1095 Mirror-like faults and power dissipation during earthquakes. *Geology*, *41*(11), 1175-
1096 1178. Retrieved from <https://doi.org/10.1130/G34641.1> doi: 10.1130/G34641.1
- 1097 Fukuyama, E., Tsuchida, K., Kawakata, H., Yamashita, F., Mizoguchi, K., & Xu, S.
1098 (2018). Spatiotemporal complexity of 2-D rupture nucleation process observed by
1099 direct monitoring during large-scale biaxial rock friction experiments. *Tectono-*
1100 *physics*, *733*, 182 - 192. Retrieved from [http://www.sciencedirect.com/science/](http://www.sciencedirect.com/science/article/pii/S0040195117305267)
1101 [article/pii/S0040195117305267](http://www.sciencedirect.com/science/article/pii/S0040195117305267) (Physics of Earthquake Rupture Propagation)

- doi: <https://doi.org/10.1016/j.tecto.2017.12.023>
- Galvez, P., Dalguer, L. A., Ampuero, J. P., & Giardini, D. (2016). Rupture Reactivation during the 2011 Mw 9.0 Tohoku Earthquake: Dynamic Rupture and Ground-Motion Simulations. *Bulletin of the Seismological Society of America*, *106*(3), 819. Retrieved from <http://dx.doi.org/10.1785/0120150153> doi: 10.1785/0120150153
- Goebel, T. H. W., Schorlemmer, D., Becker, T. W., Dresen, G., & Sammis, C. G. (2013, September). Acoustic emissions document stress changes over many seismic cycles in stick-slip experiments. *Geophys. Res. Lett.*, *40*(10), 2049–2054. Retrieved from <https://doi.org/10.1002/grl.50507> doi: 10.1002/grl.50507
- Goldberg, R., Siman-Tov, S., & Emmanuel, S. (2016). Weathering resistance of carbonate fault mirrors promotes rupture localization. *Geophysical Research Letters*, *43*(7), 3105–3111. Retrieved from <http://dx.doi.org/10.1002/2016GL067788> (2016GL067788) doi: 10.1002/2016GL067788
- Gonzalez, R. C., Woods, R., & Eddins, S. L. (2009). *Digital Image Processing Using MATLAB*. Gatesmark Publishing.
- Greenwood, J. A., & Williamson, J. B. P. (1966). Contact of Nominally Flat Surfaces. *Proceedings of the Royal Society of London A*, *295*(1442), 300–319. doi: 10.1098/rspa.1966.0242
- Gulia, L., Tormann, T., Wiemer, S., Herrmann, M., & Seif, S. (2016). Short-term probabilistic earthquake risk assessment considering time-dependent b values. *Geophysical Research Letters*, *43*(3), 1100–1108. Retrieved from <http://dx.doi.org/10.1002/2015GL066686> (2015GL066686) doi: 10.1002/2015GL066686
- Gulia, L., & Wiemer, S. (2019). Real-time discrimination of earthquake foreshocks and aftershocks. *Nature*, *574*, 193–199.
- He, D., Zhou, P., Yan, Y., Kang, R., & Guo, D. (2017). Nonlinear Compression Behavior of the Grooved Polishing Pad: A Model and Its Validation. *ECS Journal of Solid State Science and Technology*, *6*(4), 178–183.
- Heaton, T. H. (1990). Evidence for and implications of self-healing pulses of slip in earthquake rupture. *Physics of the Earth and Planetary Interiors*, *64*(1), 1–20. Retrieved from <http://www.sciencedirect.com/science/article/pii/003192019090002F> doi: [http://dx.doi.org/10.1016/0031-9201\(90\)90002-F](http://dx.doi.org/10.1016/0031-9201(90)90002-F)
- Hillers, G., Mai, P. M., Ben-Zion, Y., & Ampuero, J.-P. (2007, 05). Statistical properties of seismicity of fault zones at different evolutionary stages. *Geophysical Jour-*

- 1135 *nal International*, 169(2), 515–533. Retrieved from [https://doi.org/10.1111/](https://doi.org/10.1111/j.1365-246X.2006.03275.x)
 1136 [j.1365-246X.2006.03275.x](https://doi.org/10.1111/j.1365-246X.2006.03275.x) doi: 10.1111/j.1365-246X.2006.03275.x
- 1137 Horowitz, F. G., & Ruina, A. (1989). Slip patterns in a spatially homogeneous
 1138 fault model. *Journal of Geophysical Research: Solid Earth*, 94(B8), 10279–
 1139 10298. Retrieved from [https://agupubs.onlinelibrary.wiley.com/doi/abs/10](https://agupubs.onlinelibrary.wiley.com/doi/abs/10.1029/JB094iB08p10279)
 1140 [.1029/JB094iB08p10279](https://agupubs.onlinelibrary.wiley.com/doi/abs/10.1029/JB094iB08p10279) doi: 10.1029/JB094iB08p10279
- 1141 Hu, S., Huang, W., Shi, X., Peng, Z., & Liu, X. (2019a, June). Bi-fractal feature of bi-
 1142 Gaussian stratified surfaces. *Tribology International*, 134, 427–434. Retrieved from
 1143 <http://www.sciencedirect.com/science/article/pii/S0301679X19300854>
- 1144 Hu, S., Huang, W., Shi, X., Peng, Z., & Liu, X. (2019b, March). Mechanism of bi-gaussian
 1145 surface topographies on generating acoustic emissions under a sliding friction. *Tri-*
 1146 *bulogy International*, 131, 64–72. Retrieved from [http://www.sciencedirect.com/](http://www.sciencedirect.com/science/article/pii/S0301679X18304961)
 1147 [science/article/pii/S0301679X18304961](http://www.sciencedirect.com/science/article/pii/S0301679X18304961)
- 1148 Ide, S. (2019). Frequent observations of identical onsets of large and small earthquakes.
 1149 *Nature*, 573, 112–116.
- 1150 Ide, S., & Aochi, H. (2005). Earthquakes as multiscale dynamic ruptures with heterogeneous
 1151 fracture surface energy. *Journal of Geophysical Research: Solid Earth*, 110(B11), n/a–
 1152 n/a. Retrieved from <http://dx.doi.org/10.1029/2004JB003591> doi: 10.1029/
 1153 [2004JB003591](http://dx.doi.org/10.1029/2004JB003591)
- 1154 Iio, Y. (1995). Observations of the slow initial phase generated by microearthquakes: Impli-
 1155 cations for earthquake nucleation and propagation. *Journal of Geophysical Research*,
 1156 100(B8), 15333–15349. doi: 10.1029/95JB01150
- 1157 Johnson, K. L. (1985). *Contact Mechanics*. Cambridge University Press.
- 1158 Kammer, D. S., Radiguet, M., Ampuero, J.-P., & Molinari, J.-F. (2015, Jan 23). Linear Elas-
 1159 tic Fracture Mechanics Predicts the Propagation Distance of Frictional Slip. *Tribology*
 1160 *Letters*, 57(3), 23. Retrieved from <https://doi.org/10.1007/s11249-014-0451-8>
 1161 doi: 10.1007/s11249-014-0451-8
- 1162 Kammer, D. S., Yastrebov, V. A., Spijker, P., & Molinari, J.-F. (2012, Oct 01). On
 1163 the Propagation of Slip Fronts at Frictional Interfaces. *Tribology Letters*, 48(1), 27–
 1164 32. Retrieved from <https://doi.org/10.1007/s11249-012-9920-0> doi: 10.1007/
 1165 [s11249-012-9920-0](https://doi.org/10.1007/s11249-012-9920-0)
- 1166 Kaneko, Y., & Ampuero, J.-P. (2011). A mechanism for preseismic steady rupture fronts
 1167 observed in laboratory experiments. *Geophysical Research Letters*, 38(21). doi: 10

- 1168 .1029/2011GL049953
- 1169 Kaneko, Y., Avouac, J.-P., & Lapusta, N. (2010, May). Towards inferring earthquake
1170 patterns from geodetic observations of interseismic coupling. *Nature Geoscience*, *3*(5),
1171 363–369. Retrieved from <https://doi.org/10.1038/ngeo843>
- 1172 Kaneko, Y., Nielsen, S. B., & Carpenter, B. M. (2016). The onset of laboratory earthquakes
1173 explained by nucleating rupture on a rate-and-state fault. *Journal of Geophysical
1174 Research: Solid Earth*, *121*(8), 6071–6091. doi: 10.1002/2016JB013143
- 1175 Kaneko, Y., & Shearer, P. M. (2015). Variability of seismic source spectra, estimated
1176 stress drop, and radiated energy, derived from cohesive-zone models of symmetrical
1177 and asymmetrical circular and elliptical ruptures. *Journal of Geophysical Research:
1178 Solid Earth*, *120*(2), 1053–1079. Retrieved from [https://agupubs.onlinelibrary
1179 .wiley.com/doi/abs/10.1002/2014JB011642](https://agupubs.onlinelibrary.wiley.com/doi/abs/10.1002/2014JB011642) doi: 10.1002/2014JB011642
- 1180 Kato, A., Fukuda, J., Kumazawa, T., & Nakagawa, S. (2016). Accelerated nucleation
1181 of the 2014 Iquique, Chile Mw 8.2 Earthquake. *Scientific Reports*, *6*(24792). doi:
1182 doi:10.1038/srep24792
- 1183 Kato, A., Obara, K., Igarashi, T., Hiroshi, T., Nakagawa, S., & Hirata, N. (2012). Propa-
1184 gation of Slow Slip Leading Up to the 2011 Mw 9.0 Tohoku-Oki Earthquake. *Science*,
1185 *335*, 705–708.
- 1186 Kato, N. (2003). Repeating Slip Events at a Circular Asperity: Numerical Simulation with
1187 a Rate- and State-Dependent Friction Law. *Bull. Earthq. Res. Inst. Univ. Tokyo*, *78*,
1188 151–166.
- 1189 Ke, C.-Y., McLaskey, G. C., & Kammer, D. S. (2018). Rupture Termination in Laboratory-
1190 Generated Earthquakes. *Geophysical Research Letters*, *45*(23), 12,784–12,792. doi:
1191 10.1029/2018GL080492
- 1192 Kirkpatrick, J. D., & Brodsky, E. E. (2014). Slickensite orientations as a record of fault rock
1193 rheology. *Earth and Planetary Science Letters*, *408*, 24–34. doi: [http://dx.doi.org/
1194 10.1016/j.epsl.2014.09.040](http://dx.doi.org/10.1016/j.epsl.2014.09.040)
- 1195 Kirkpatrick, J. D., Rowe, C. D., White, J. C., & Brodsky, E. E. (2013). Silica gel formation
1196 during fault slip: Evidence from the rock record. *Geology*, *41*(9), 1015–1018. Retrieved
1197 from <https://doi.org/10.1130/G34483.1>
- 1198 Latour, S., Schubnel, A., Nielsen, S., Madariaga, R., & Vinciguerra, S. (2013). Charac-
1199 terization of nucleation during laboratory earthquakes. *Geophysical Research Letters*,
1200 *40*(19), 5064–5069. doi: 10.1002/grl.50974

- 1201 Leefe, S. E., Dowson, D., Taylor, C. M., Childs, T. H. C., Dalmaz, G., Berthier, Y., ...
1202 Lubrecht, A. A. (1998, January). “Bi-Gaussian” representation of worn surface to-
1203 pography in elastic contact problems. In *Tribology series* (Vol. 34, pp. 281–290).
1204 Elsevier. Retrieved from [http://www.sciencedirect.com/science/article/pii/](http://www.sciencedirect.com/science/article/pii/S0167892298800837)
1205 [S0167892298800837](http://www.sciencedirect.com/science/article/pii/S0167892298800837)
- 1206 Luo, Y., Ampuero, J. P., Galvez, P., van den Ende, M., & Idini, B. (2017). QDYN:
1207 a Quasi-DYNamic earthquake simulator (v1.1) [Computer software manual]. doi:
1208 [10.5281/zenodo.322459](https://doi.org/10.5281/zenodo.322459)
- 1209 Ma, S., Ma, J., & Liu, L. (2002). Experimental evidence for seismic nucleation phase. *Chin.*
1210 *Sci. Bull.*, *47*, 769–773. doi: <https://doi.org/10.1360/02tb9174>
- 1211 Madariaga, R. (1976). Dynamics of an expanding circular fault. *Bulletin of the Seismological*
1212 *Society of America*, *66*(3), 639. Retrieved from <http://dx.doi.org/>
- 1213 Maegawa, S., Suzuki, A., & Nakano, K. (2010, Jun 01). Precursors of Global Slip in a Lon-
1214 gitudinal Line Contact Under Non-Uniform Normal Loading. *Tribology Letters*, *38*(3),
1215 313–323. Retrieved from <https://doi.org/10.1007/s11249-010-9611-7> doi:
1216 [10.1007/s11249-010-9611-7](https://doi.org/10.1007/s11249-010-9611-7)
- 1217 Mai, P. M., & Beroza, G. C. (2002). A spatial random field model to character-
1218 ize complexity in earthquake slip. *Journal of Geophysical Research: Solid Earth*,
1219 *107*(B11), 2308. Retrieved from <http://dx.doi.org/10.1029/2001JB000588> doi:
1220 [10.1029/2001JB000588](http://dx.doi.org/10.1029/2001JB000588)
- 1221 Mai, P. M., Galis, M., Thingbaijam, K. K. S., Vyas, J. C., & Dunham, E. M. (2018).
1222 Accounting for Fault Roughness in Pseudo-Dynamic Ground-Motion Simulations. In
1223 L. A. Dalguer, Y. Fukushima, K. Irikura, & C. Wu (Eds.), *Best practices in physics-*
1224 *based fault rupture models for seismic hazard assessment of nuclear installations* (pp.
1225 95–126). Cham: Springer International Publishing. Retrieved from [https://doi.org/](https://doi.org/10.1007/978-3-319-72709-7_7)
1226 [10.1007/978-3-319-72709-7_7](https://doi.org/10.1007/978-3-319-72709-7_7) doi: [10.1007/978-3-319-72709-7_7](https://doi.org/10.1007/978-3-319-72709-7_7)
- 1227 Mai, P. M., Somerville, P., Pitarka, A., Dalguer, L., Song, S., Beroza, G., ... Irikura,
1228 K. (2006). On Scaling of Fracture Energy and Stress Drop in Dynamic Rup-
1229 ture Models: Consequences for Near-Source Ground-Motions. In *Earthquakes: Ra-*
1230 *diated energy and the physics of faulting* (pp. 283–293). American Geophysical
1231 Union (AGU). Retrieved from [https://agupubs.onlinelibrary.wiley.com/doi/](https://agupubs.onlinelibrary.wiley.com/doi/abs/10.1029/170GM28)
1232 [abs/10.1029/170GM28](https://agupubs.onlinelibrary.wiley.com/doi/abs/10.1029/170GM28) doi: [10.1029/170GM28](https://doi.org/10.1029/170GM28)
- 1233 Marone, C., & Cox, S. J. D. (1994). Scaling of rock friction constitutive parameters: The

- 1234 effects of surface roughness and cumulative offset on friction of gabbro. *Pure and*
 1235 *Applied Geophysics*, 143(1-3), 359–385. doi: 10.1007/BF00874335
- 1236 McGuire, J. J., & Kaneko, Y. (2018). Directly estimating earthquake rupture area using
 1237 second moments to reduce the uncertainty in stress drop. *Geophysical Journal Interna-*
 1238 *tional*, 214(3), 2224–2235. Retrieved from <http://dx.doi.org/10.1093/gji/ggy201>
 1239 doi: 10.1093/gji/ggy201
- 1240 McLaskey, G. C. (2019). Earthquake Initiation From Laboratory Observations and Im-
 1241 plications for Foreshocks. *Journal of Geophysical Research: Solid Earth*, 124(12),
 1242 12882–12904. Retrieved from [https://agupubs.onlinelibrary.wiley.com/doi/](https://agupubs.onlinelibrary.wiley.com/doi/abs/10.1029/2019JB018363)
 1243 [abs/10.1029/2019JB018363](https://agupubs.onlinelibrary.wiley.com/doi/abs/10.1029/2019JB018363) doi: 10.1029/2019JB018363
- 1244 McLaskey, G. C., & Kilgore, B. D. (2013). Foreshocks during the nucleation of stick-
 1245 slip instability. *Journal of Geophysical Research*, 118(6), 2982–2997. doi: 10.1002/
 1246 jgrb.50232
- 1247 McLaskey, G. C., Kilgore, B. D., Lockner, D. A., & Beeler, N. M. (2014). Laboratory
 1248 Generated M -6 Earthquakes. *Pure and Applied Geophysics*. doi: 10.1007/s00024-013-
 1249 -0772-9
- 1250 McLaskey, G. C., & Lockner, D. A. (2014). Preslip and cascade processes initiating
 1251 laboratory stick slip. *Journal of Geophysical Research: Solid Earth*, 119(8), 6323–
 1252 6336. Retrieved from <http://dx.doi.org/10.1002/2014JB011220> doi: 10.1002/
 1253 2014JB011220
- 1254 Meier, M.-A., Heaton, T., & Clinton, J. (2016). Evidence for universal earthquake rupture
 1255 initiation behavior. *Geophysical Research Letters*, 43(15), 7991–7996. doi: 10.1002/
 1256 2016GL070081
- 1257 Mignan, A. (2012). Functional shape of the earthquake frequency-magnitude distribu-
 1258 tion and completeness magnitude. *Journal of Geophysical Research: Solid Earth*,
 1259 117(B8). Retrieved from [https://agupubs.onlinelibrary.wiley.com/doi/abs/](https://agupubs.onlinelibrary.wiley.com/doi/abs/10.1029/2012JB009347)
 1260 [10.1029/2012JB009347](https://agupubs.onlinelibrary.wiley.com/doi/abs/10.1029/2012JB009347) doi: 10.1029/2012JB009347
- 1261 Mignan, A. (2014). The debate on the prognostic value of earthquake foreshocks: A meta-
 1262 analysis. *Scientific Reports*, 4, 4099.
- 1263 Mignan, A. (2020). Asymmetric Laplace Mixture Modelling of Incomplete Power-Law
 1264 Distributions: Application to ‘Seismicity Vision’. In K. Arai & S. Kapoor (Eds.),
 1265 *Advances in computer vision* (pp. 30–43). Cham: Springer International Publishing.
- 1266 Mogi, K. (1963). Some Discussions on Aftershocks, Foreshocks and Earthquake Swarms:

- 1267 the Fracture of a Semi-infinite Body Caused by an Inner Stress Origin and Its Relation
 1268 to the Earthquake Phenomena (Third Paper). *Bulletin of the Earthquake Research*
 1269 *Institute*, 41, 615–658.
- 1270 Mogi, K. (1985). *Earthquake prediction*. Academic Press Japan.
- 1271 Nadeau, R. M., Antolik, M., Johnson, P. A., Foxall, W., & McEvilly, T. V. (1994). Seis-
 1272 mological studies at Parkfield III: Microearthquake clusters in the study of fault-zone
 1273 dynamics. *Bulletin of the Seismological Society of America*, 84(2), 247–263.
- 1274 Nadeau, R. M., & McEvilly, T. V. (1999). Fault Slip Rates at Depth from Recurrence
 1275 Intervals of Repeating Microearthquakes. *Science*, 285(5428), 718–721. doi: 10.1126/
 1276 science.285.5428.718
- 1277 Nielsen, S., Taddeucci, J., & Vinciguerra, S. (2010). Experimental observation of stick-slip
 1278 instability fronts. *Geophysical Journal International*, 180(2), 697–702. doi: 10.1111/
 1279 j.1365-246X.2009.04444.x
- 1280 Noda, H., Nakatani, M., & Hori, T. (2013). Large nucleation before large earthquakes is
 1281 sometimes skipped due to cascade-up – Implications from a rate and state simulation
 1282 of faults with hierarchical asperities. *Journal of Geophysical Research: Solid Earth*,
 1283 118(6), 2924–2952. Retrieved from [https://agupubs.onlinelibrary.wiley.com/
 1284 doi/abs/10.1002/jgrb.50211](https://agupubs.onlinelibrary.wiley.com/doi/abs/10.1002/jgrb.50211) doi: 10.1002/jgrb.50211
- 1285 Obara, K., & Kato, A. (2016). Connecting slow earthquakes to huge earthquakes. *Science*,
 1286 353(6296), 253–257. doi: 10.1126/science.aaf1512
- 1287 Ohnaka, M. (1992). Earthquake source nucleation: A physical model for short-term pre-
 1288 cursors. *Tectonophysics*, 211(1-4), 149–178. doi: dx.doi.org/10.1016/0040-1951(92)
 1289 90057-D
- 1290 Ohnaka, M., & Shen, L. F. (1999). Scaling of the shear rupture process from nucleation to
 1291 dynamic propagation: Implications of geometric irregularity of the rupturing surfaces.
 1292 *Journal of Geophysical Research*, 104(B1), 817–844. doi: 10.1029/1998JB900007
- 1293 Okubo, P. G., & Dieterich, J. H. (1984). Effects of physical fault properties on frictional
 1294 instabilities produced on simulated faults. *Journal of Geophysical Research*, 89(B7),
 1295 5817–5827. doi: 10.1029/JB089iB07p05817
- 1296 Okuda, T., & Ide, S. (2018a). Hierarchical rupture growth evidenced by the initial seismic
 1297 waveforms. *Nature Communications*, 9(3714).
- 1298 Okuda, T., & Ide, S. (2018b, August). Streak and hierarchical structures of the Tohoku-
 1299 Hokkaido subduction zone plate boundary. *Earth, Planets and Space*, 70(1), 132.

- 1300 Retrieved from <https://doi.org/10.1186/s40623-018-0903-8>
- 1301 Ozawa, S. W., Hatano, T., & Kame, N. (2019). Longer Migration and Spontaneous Decay of
1302 Aseismic Slip Pulse Caused by Fault Roughness. *Geophysical Research Letters*, *46*(2),
1303 636–643. doi: 10.1029/2018GL081465
- 1304 Passelègue, F. X., Latour, S., Schubnel, A., Nielsen, S., Bhat, H. S., & Madariaga, R.
1305 (2017). Influence of Fault Strength on Precursory Processes During Laboratory
1306 Earthquakes. In *Fault zone dynamic processes* (pp. 229–242). American Geophys-
1307 ical Union (AGU). Retrieved from [https://agupubs.onlinelibrary.wiley.com/](https://agupubs.onlinelibrary.wiley.com/doi/abs/10.1002/9781119156895.ch12)
1308 [doi/abs/10.1002/9781119156895.ch12](https://agupubs.onlinelibrary.wiley.com/doi/abs/10.1002/9781119156895.ch12) doi: 10.1002/9781119156895.ch12
- 1309 Pawlus, P. (2008, March). Simulation of stratified surface topographies. *Wear*, *264*(5),
1310 457–463. Retrieved from [http://www.sciencedirect.com/science/article/pii/](http://www.sciencedirect.com/science/article/pii/S0043164807002062)
1311 [S0043164807002062](http://www.sciencedirect.com/science/article/pii/S0043164807002062)
- 1312 Persson, B. N. J. (2006). Contact mechanics for randomly rough surfaces. *Surface Science*
1313 *Reports*, *61*(4), 201–227. doi: 10.1016/j.surfrep.2006.04.001
- 1314 Plummakers, A., & Røyne, A. (2017, October). Nanograin formation and reaction-
1315 induced fracturing due to decarbonation: Implications for the microstructures of
1316 fault mirrors. *Earth and Planetary Science Letters*, *476*, 59–68. Retrieved from
1317 <http://www.sciencedirect.com/science/article/pii/S0012821X17304387>
- 1318 Power, W. L., & Tullis, T. E. (1991). Euclidean and fractal models for the description
1319 of rock surface roughness. *Journal of Geophysical Research*, *96*(B1), 415–424. doi:
1320 10.1029/90JB02107
- 1321 Pozzi, G., De Paola, N., Nielsen, S. B., Holdsworth, R. E., & Bowen, L. (2018). A new
1322 interpretation for the nature and significance of mirror-like surfaces in experimental
1323 carbonate-hosted seismic faults. *Geology*, *46*(7), 583. doi: 10.1130/G40197.1
- 1324 Ranjith, K., & Rice, J. R. (1999). Stability of quasi-static slip in a single degree of freedom
1325 elastic system with rate and state dependent friction. *Journal of the Mechanics and*
1326 *Physics of Solids*, *47*(6), 1207–1218. Retrieved from [http://www.sciencedirect](http://www.sciencedirect.com/science/article/pii/S0022509698001136)
1327 [.com/science/article/pii/S0022509698001136](http://www.sciencedirect.com/science/article/pii/S0022509698001136) doi: [https://doi.org/10.1016/](https://doi.org/10.1016/S0022-5096(98)00113-6)
1328 [S0022-5096\(98\)00113-6](https://doi.org/10.1016/S0022-5096(98)00113-6)
- 1329 Renard, F., Voisin, C., Marsan, D., & Schmittbuhl, J. (2006, August). High resolution 3D
1330 laser scanner measurements of a strike-slip fault quantify its morphological anisotropy
1331 at all scales. *Geophysical Research Letters*, *33*(4), L04305. Retrieved from [https://](https://doi.org/10.1029/2005GL025038)
1332 doi.org/10.1029/2005GL025038 doi: 10.1029/2005gl025038

- 1333 Rice, J. R. (1993). Spatio-temporal complexity of slip on a fault. *Journal of Geophysical*
 1334 *Research: Solid Earth*, *98*(B6), 9885–9907. doi: 10.1029/93JB00191
- 1335 Roeloffs, E. A. (2006). Evidence for aseismic deformation rate changes prior to earth-
 1336 quakes. *Annual Review of Earth and Planetary Sciences*, *34*(1), 591-627. Re-
 1337 trieved from <https://doi.org/10.1146/annurev.earth.34.031405.124947> doi:
 1338 10.1146/annurev.earth.34.031405.124947
- 1339 Rubin, A. M., & Ampuero, J. P. (2005). Earthquake nucleation on (aging) rate and state
 1340 faults. *Journal of Geophysical Research: Solid Earth*, *110*(B11), n/a–n/a. Retrieved
 1341 from <http://dx.doi.org/10.1029/2005JB003686> doi: 10.1029/2005JB003686
- 1342 Rubinstein, S. M., Cohen, G., & Fineberg, J. (2004). Detachment fronts and the onset of
 1343 dynamic friction. *Nature*, *430*, 1005–1009. doi: 10.1038/nature02830
- 1344 Rubinstein, S. M., Shay, M., Cohen, G., & Fineberg, J. (2006). Crack-like processes
 1345 governing the onset of frictional slip. *International Journal of Fracture*, *140*(1-4),
 1346 201–212. doi: 10.1007/s10704-006-0049-8
- 1347 Ruina, A. (1983). Slip instability and state variable friction laws. *Journal of Geophysical*
 1348 *Research*, *88*(B12), 10,359–10,370. doi: 10.1029/JB088iB12p10359
- 1349 Ruiz, S., Metois, M., Fuenzalida, A., Ruiz, J., Leyton, F., Grandin, R., ... Campos, J.
 1350 (2014). Intense foreshocks and a slow slip event preceded the 2014 Iquique Mw 8.1
 1351 earthquake. *Science*, *345*(6201), 1165–1169. Retrieved from [http://www.sciencemag](http://www.sciencemag.org/content/345/6201/1165.abstract)
 1352 [.org/content/345/6201/1165.abstract](http://www.sciencemag.org/content/345/6201/1165.abstract) doi: 10.1126/science.1256074
- 1353 Schmittbuhl, J., Chambon, G., Hansen, A., & Bouchon, M. (2006). Are stress distributions
 1354 along faults the signature of asperity squeeze? *Geophysical Research Letters*, *33*(13),
 1355 L13307.
- 1356 Schmittbuhl, J., Vilotte, J.-P., & Roux, S. (1995, Jan). Reliability of self-affine measure-
 1357 ments. *Phys. Rev. E*, *51*, 131–147. Retrieved from [https://link.aps.org/doi/](https://link.aps.org/doi/10.1103/PhysRevE.51.131)
 1358 [10.1103/PhysRevE.51.131](https://link.aps.org/doi/10.1103/PhysRevE.51.131) doi: 10.1103/PhysRevE.51.131
- 1359 Scholz, C. H. (1997, 08). Size distributions for large and small earthquakes. *Bulletin of the*
 1360 *Seismological Society of America*, *87*(4), 1074-1077.
- 1361 Scholz, C. H. (2002). *The Mechanics of Earthquakes and Faulting* (2nd ed.). UK: Cambridge
 1362 University Press.
- 1363 Scholz, C. H., & Aviles, C. A. (1986). The Fractal Geometry of Faults and Faulting. In
 1364 *Earthquake source mechanics* (pp. 147–155). American Geophysical Union (AGU).
 1365 doi: 10.1029/GM037p0147

- 1366 Seif, S., Zechar, J. D., Mignan, S., A. and Nandan, & Wiemer, S. (2018, 12). Foreshocks and
 1367 Their Potential Deviation from General Seismicity. *Bulletin of the Seismological Soci-*
 1368 *ety of America*, 109(1), 1-18. Retrieved from <https://doi.org/10.1785/0120170188>
 1369 doi: 10.1785/0120170188
- 1370 Selvadurai, P. A. (2015). *Laboratory studies of frictional sliding and the implications of*
 1371 *precursory seismicity* (phdthesis, Univerity of California, Berkeley). Retrieved from
 1372 <https://escholarship.org/uc/item/4xm835kb>
- 1373 Selvadurai, P. A. (2019). Laboratory insight into seismic estimates of energy partitioning
 1374 during dynamic rupture: An observable scaling breakdown. *Journal of Geophysical*
 1375 *Research: Solid Earth*.
- 1376 Selvadurai, P. A., & Glaser, S. D. (2015a). Laboratory-developed Contact Models Con-
 1377 trolling Instability on Frictional Faults. *Journal of Geophysical Research*, 120(6),
 1378 4208–4236. doi: 10.1002/2014JB011690
- 1379 Selvadurai, P. A., & Glaser, S. D. (2015b). Novel Monitoring Techniques for Characterizing
 1380 Frictional Interfaces in the Laboratory. *Sensors*, 15(5), 9791–9814. doi: 10.3390/
 1381 s150509791
- 1382 Selvadurai, P. A., & Glaser, S. D. (2017). Asperity generation and its relationship to seis-
 1383 micity on a planar fault: A laboratory simulation. *Geophysical Journal International*,
 1384 208, 1009–1025. doi: doi:10.1093/gji/ggw439
- 1385 Selvadurai, P. A., Glaser, S. D., & Parker, J. M. (2017). On factors controlling precursor slip
 1386 fronts in the laboratory and their relation to slow slip events in nature. *Geophysical*
 1387 *Research Letters*, 44. Retrieved from <http://dx.doi.org/10.1002/2017GL072538>
 1388 doi: 10.1002/2017GL072538
- 1389 Shirzaei, M., & Bürgmann, R. (2013). Time-dependent model of creep on the Hayward
 1390 fault from joint inversion of 18 years of InSAR and surface creep data. *Journal of*
 1391 *Geophysical Research*, 118, 1733–1746. doi: 10.1002/jgrb.50149
- 1392 Siman-Tov, S., Aharonov, E., Boneh, Y., & Reches, Z. (2015). Fault mirrors along carbonate
 1393 faults: Formation and destruction during shear experiments. *Earth and Planetary*
 1394 *Science Letters*, 430, 367–376. Retrieved from [http://www.sciencedirect.com/](http://www.sciencedirect.com/science/article/pii/S0012821X15005579)
 1395 [science/article/pii/S0012821X15005579](http://www.sciencedirect.com/science/article/pii/S0012821X15005579) doi: <http://doi.org/10.1016/j.epsl.2015>
 1396 .08.031
- 1397 Siman-Tov, S., Aharonov, E., Sagy, A., & Emmanuel, S. (2013). Nanograins form carbonate
 1398 fault mirrors. *Geology*, 41(6), 703–706.

- 1399 Siman-Tov, S., Stock, G. M., Brodsky, E. E., & White, J. C. (2017). The coating layer of
1400 glacial polish. *Geology*, *45*(11), 987–990. Retrieved from [https://doi.org/10.1130/](https://doi.org/10.1130/G39281.1)
1401 [G39281.1](https://doi.org/10.1130/G39281.1)
- 1402 Socquet, A., Valdes, J. P., Jara, J., Cotton, F., Walpersdorf, A., Cotte, N., . . . Norabuena,
1403 E. (2017). An 8 month slow slip event triggers progressive nucleation of the 2014
1404 Chile megathrust. *Geophysical Research Letters*, *44*(9), 4046–4053. doi: 10.1002/
1405 2017GL073023
- 1406 Svetlizky, I., & Fineberg, J. (2014). Classical shear cracks drive the onset of dry frictional
1407 motion. *Nature*, *509*, 205–209.
- 1408 Tal, Y., Hager, B. H., & Ampuero, J. P. (2018). The Effects of Fault Roughness on
1409 the Earthquake Nucleation Process. *Journal of Geophysical Research: Solid Earth*,
1410 *123*(1), 437–456. doi: 10.1002/2017JB014746
- 1411 Tinti, E., Spudich, P., & Cocco, M. (2005). Earthquake fracture energy inferred from
1412 kinematic rupture models on extended faults. *Journal of Geophysical Research:*
1413 *Solid Earth*, *110*(B12), n/a–n/a. Retrieved from [http://dx.doi.org/10.1029/](http://dx.doi.org/10.1029/2005JB003644)
1414 [2005JB003644](http://dx.doi.org/10.1029/2005JB003644) (B12303) doi: 10.1029/2005JB003644
- 1415 Tisato, N., Di Toro, G., De Rossi, N., Quaresimin, M., & Candela, T. (2012). Exper-
1416 imental investigation of flash weakening in limestone. *Journal of Structural Ge-*
1417 *ology*, *38*, 183 - 199. Retrieved from [http://www.sciencedirect.com/science/](http://www.sciencedirect.com/science/article/pii/S0191814111002057)
1418 [article/pii/S0191814111002057](http://www.sciencedirect.com/science/article/pii/S0191814111002057) (Physico-Chemical Processes in Seismic Faults)
1419 doi: <https://doi.org/10.1016/j.jsg.2011.11.017>
- 1420 Tormann, T., Enescu, B., Woessner, J., & Wiemer, S. (2015). Randomness of megathrust
1421 earthquakes implied by rapid stress recovery after the Japan earthquake. *Nature*
1422 *Geoscience*, *8*, 152–158.
- 1423 Tormann, T., Wiemer, S., & Mignan, A. (2014). Systematic survey of high-resolution b
1424 value imaging along Californian faults: Inference on asperities. *Journal of Geophysical*
1425 *Research: Solid Earth*, *119*(3), 2029–2054. Retrieved from [http://dx.doi.org/10](http://dx.doi.org/10.1002/2013JB010867)
1426 [.1002/2013JB010867](http://dx.doi.org/10.1002/2013JB010867) doi: 10.1002/2013JB010867
- 1427 Trømborg, J., Scheibert, J., Amundsen, D. S., Thøgersen, K., & Malthe-Sørenssen, A.
1428 (2011). Transition from static to kinetic friction: Insights from a 2D model. *Physical*
1429 *Review Letters*, *107*, 074301.
- 1430 Uchida, N. (2019). Detection of repeating earthquakes and their application in characterizing
1431 slow fault slip. *Progress in Earth and Planetary Science*, *6*(40). Retrieved from

- 1432 <https://doi.org/10.1186/s40645-019-0284-z>
- 1433 Verberne, B. A., Plumper, O., & Spiers, C. J. (2019). Nanocrystalline Principal Slip Zones
1434 and Their Role in Controlling Crustal Fault Rheology. *Minerals*, *9*, 328.
- 1435 Wang, K., & Bilek, S. L. (2014, January). Invited review paper: Fault creep caused
1436 by subduction of rough seafloor relief. *Tectonophysics*, *610*, 1–24. Retrieved from
1437 <http://www.sciencedirect.com/science/article/pii/S0040195113006896>
- 1438 Wiemer, S., & Wyss, M. (2002). Mapping spatial variability of the frequency-magnitude
1439 distribution of earthquakes. In R. Dmowska & B. Saltzman (Eds.), (Vol. 45, p. 259
1440 - V). Elsevier. Retrieved from <http://www.sciencedirect.com/science/article/pii/S0065268702800073> doi: [https://doi.org/10.1016/S0065-2687\(02\)80007-3](https://doi.org/10.1016/S0065-2687(02)80007-3)
- 1441 Yoshioka, N. (1997). A review of the micromechanical approach to the physics of contacting
1442 surfaces. *Tectonophysics*, *277*(1), 29–40. Retrieved from <http://www.sciencedirect.com/science/article/pii/S0040195197000760> (Earthquake Generation Pro-
1443 cesses: Environmental Aspects and Physical Modelling) doi: [https://doi.org/10.1016/S0040-1951\(97\)00076-0](https://doi.org/10.1016/S0040-1951(97)00076-0)
- 1444 Yoshioka, N., & Iwasa, K. (1996). The characteristic displacement in rate and state-
1445 dependent friction from a micromechanical point of view. *Pure and Applied Geo-*
1446 *physics*, *147*(3), 433–453. doi: 10.1007/BF00878837
- 1447 Zhuo, Y.-Q., Guo, Y., Chen, S., Ji, Y., & Ma, J. (2018). Laboratory Observations of Linkage
1448 of Preslip Zones Prior to Stick-Slip Instability. *Entropy*, *20*, 629.
- 1449 Zhuo, Y.-Q., Liu, P., Chen, S., Guo, Y., & Ma, J. (2018). Laboratory observations of
1450 tremor-like events generated during preslip. *Geophysical Research Letters*, *45*(14),
1451 6926–6934. Retrieved from [https://agupubs.onlinelibrary.wiley.com/doi/abs/](https://agupubs.onlinelibrary.wiley.com/doi/abs/10.1029/2018GL079201)
1452 [10.1029/2018GL079201](https://agupubs.onlinelibrary.wiley.com/doi/abs/10.1029/2018GL079201) doi: 10.1029/2018GL079201
1453
1454
1455